DENSITY DISTRIBUTION MEASUREMENTS
IN LARGE C.T.R. DEVICES[+]

G. Lisitano

in collaboration with

P. Morandi, B. Cannici,
E. Rossetti, N. Gottardi[++]

MAX-PLANCK-INSTITUT FÜR PLASMAPHYSIK

GARCHING BEI MÜNCHEN

DENSITY DISTRIBUTION MEASUREMENTS
IN LARGE C.T.R. DEVICES[+]

G. Lisitano

in collaboration with

P. Morandi, B. Cannici,
E. Rossetti, N. Gottardi[++]

IPP III/17   May 1975

IPP III/17

Density Distribution Measure-
ments in large C.T.R. Devices

G. Lisitano
in collaboration with
P. Morandi, B. Cannici,
E. Rossetti, N. Gottardi[+]

May 1975

Abstract

Multichannel millimetre wave interferometry has been
successfully applied to existing Tokamak discharges.
The extension of this technique to the planned larger
C.T.R. devices presents some technical problems which
are discussed on hand of the experience gained in
present day devices.

[+]Instituto di Macchine Politecnico di Milano

INTRODUCTION

One of the most important diagnostics in C.T.R. discharges
is the determination of the density profile by radiating
the plasma with several beams of electromagnetic waves. The
phase shift that each beam experiences on passing through
the plasma is related to the mean value of the plasma den-
sity along the beam, each beam furnishing one point data
for the density profile. Abel inversion of the phase shift
data gives, with a much closer approximation, the local
value of the electron density.

The choice of the frequency of the electromagnetic beams is
determined by the value of the plasma density to be
measured. The plasma should be transparent enough to the
electromagnetic beam to avoid finite path deviations of the
beam at the receiver antenna.

As we shall see, the wavelength of the electromagnetic beams
lies at millimetre and submillimetre wave range, depending
on the density value and cross-dimensions of the discharge.

In the following, firstly some representative measurements
on the Tokamak Pulsator I of IPP Garching will demonstrate
the role played by the measurement of the density profile in
understanding the discharge.

The measuring technique is then illustrated by various
examples on millimeter and submillimeter wave lengths.

I MEASUREMENTS ON THE TOKAMAK PULSATOR

An interesting aspect of the behaviour of the discharge in
the Tokamak Pulsator is determined by the conditions leading
to the disruptive instability of the induced plasma current.

Insight into the disruptive instabilities can be obtained
by relating the measurements of the discharge current with
those of the electron density distribution.

After a short description of the Tokamak Pulsator and of the
interferometric system used to measure the density distri-
bution, three representative discharge conditions will be
presented.

The first is related to a well centred discharge with no dis-
ruptive instabilities; the other two represent two cases of
disruptive instabilities obtained, the first at high value
of the density and the second at high value of the current
(runaway current).

1) Tokamak Pulsator I

Fig. 1 shows schematically the Tokamak Pulsator 1 on which
the measurements have been taken. The machine consists of a
toroidal vacuum tube of 32 cm internal diameter. The major
radius of the tube is 70 cm.

Internal to the vacuum tube is assembled a chamber of stain-
less steel of 0.3 mm thickness, which forms a tube of high
vacuum (liner). In the liner, limited by a diaphragm (limiter),
the discharge takes place. External to the vacuum tube is a
copper shell of ca. 3 cm thickness, the function of which is
to stabilise the plasma through current induced by variations
of the discharge current position. The toroidal magnetic
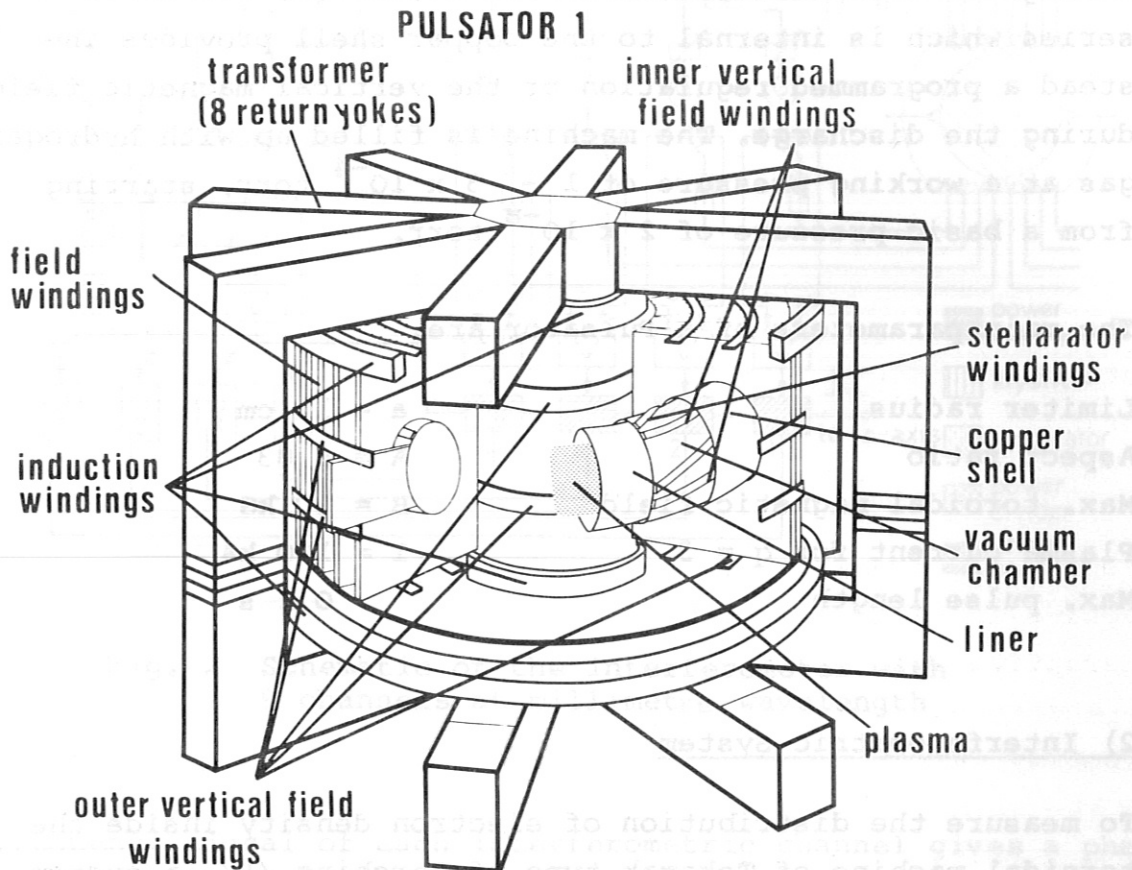field is produced by 48 water-cooled Bitter coils.

PULSATOR 1

transformer
(8 return yokes)

inner vertical
field windings

field
windings

stellarator
windings

copper
shell

induction
windings

vacuum
chamber

liner

plasma

outer vertical field
windings

Fig. 1 Tokamak Pulsator

The plasma current is induced by means of an iron core trans-
former with eight return yokes. Several primary windings are
first crowbared from high voltage capacitors in order to pre-
pare an initial plasma, which should have enough conductivity
to sustain the main discharge current crowbared from the
primary capacitor bank, having a total energy content of
235 kJ. To centre the discharge in the toroidal tube two
series of auxiliary windings are provided, producing a vertical

magnetic field to compensate that linked with the discharge
current. One of these series is external to the copper shell
and supplies a vertical field of compensation which is fixed
throughout the whole extent of the discharge; the other
series which is internal to the copper shell provides in-
stead a programmed regulation of the vertical magnetic field
during the discharge. The machine is filled up with hydrogen
gas at a working pressure of $1 - 3 \times 10^{-4}$ torr, starting
from a basic pressure of 2×10^{-8} torr.

The main parameters of a Pulsator are:

Limiter radius	$a = 12$ cm
Aspect ratio	$A = 5.83$
Max. toroidal magnetic field	$B = 30$ kG
Plasma current for $q = 3$	$I = 100$ kA
Max. pulse length	0.2 s

2) Interferometric System

To measure the distribution of electron density inside the
toroidal machine of Tokamak type of Garching /1/, a system
of 9 interferometric channels at millimetre wavelength has
been provided; the system is illustrated schematically in
Fig. 2; the working frequency of the channels can be 90 GHz
($\lambda = 3.3$ mm) or 150 GHz ($\lambda = 2$ mm).

The circuitry is based on the method of frequency transfor-
mation using sinusoidal interferometry /13/. By means of this
method it is possible, as will be seen in more detail later,
to reduce a high frequency signal (in the region of milli-
metric-submillimetric wavelength and even in the coherent
light wavelength) to a signal having any lower frequency
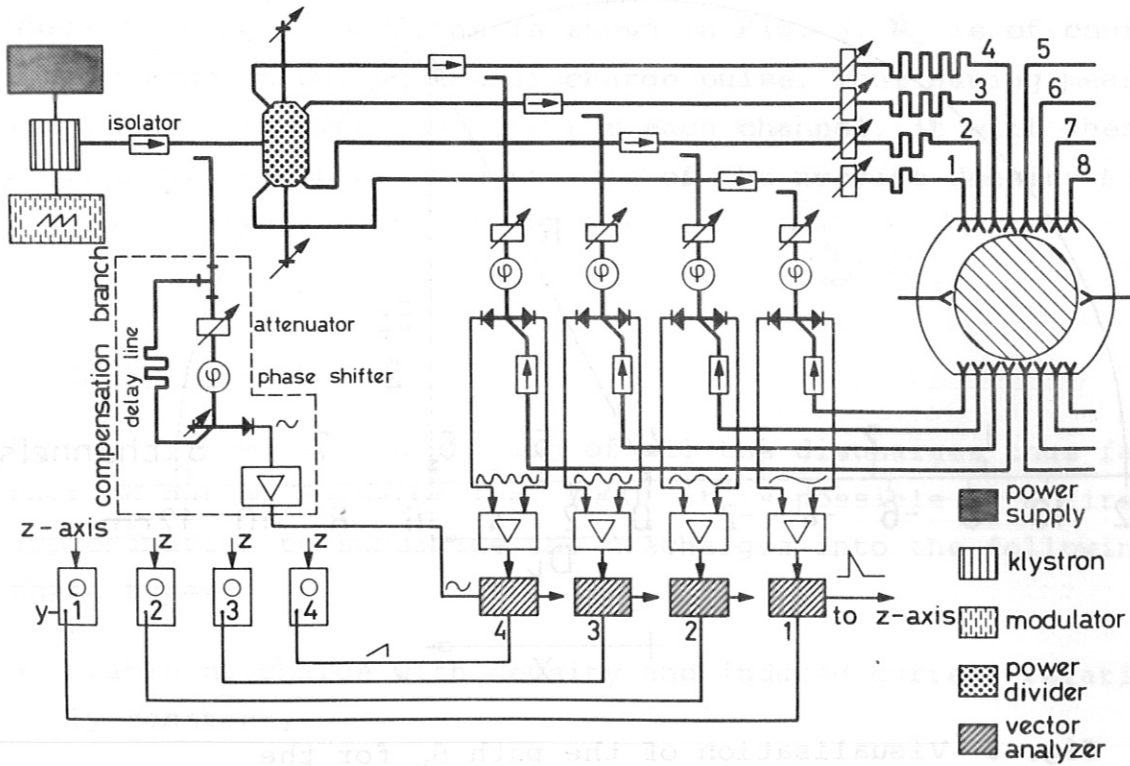without resorting to a heterodyne oscillator. The low

Fig. 2 Schematic of the interferometer with
9 channels at millimetre wavelength

frequency signal of each interferometric channel gives a phase
variation $\Delta\Phi$ which is related to the density $N(s)$ along
the path S, by the following expression:

$$\Delta\Phi = \frac{1}{2} \cdot \frac{\omega}{c} \cdot \frac{1}{N_c} \int_S N(s)\,ds \qquad (1)$$

which is valid for $N/N_c \ll 1$, where ω is the angular fre-
quency of the incident wave and N_c is the critical density
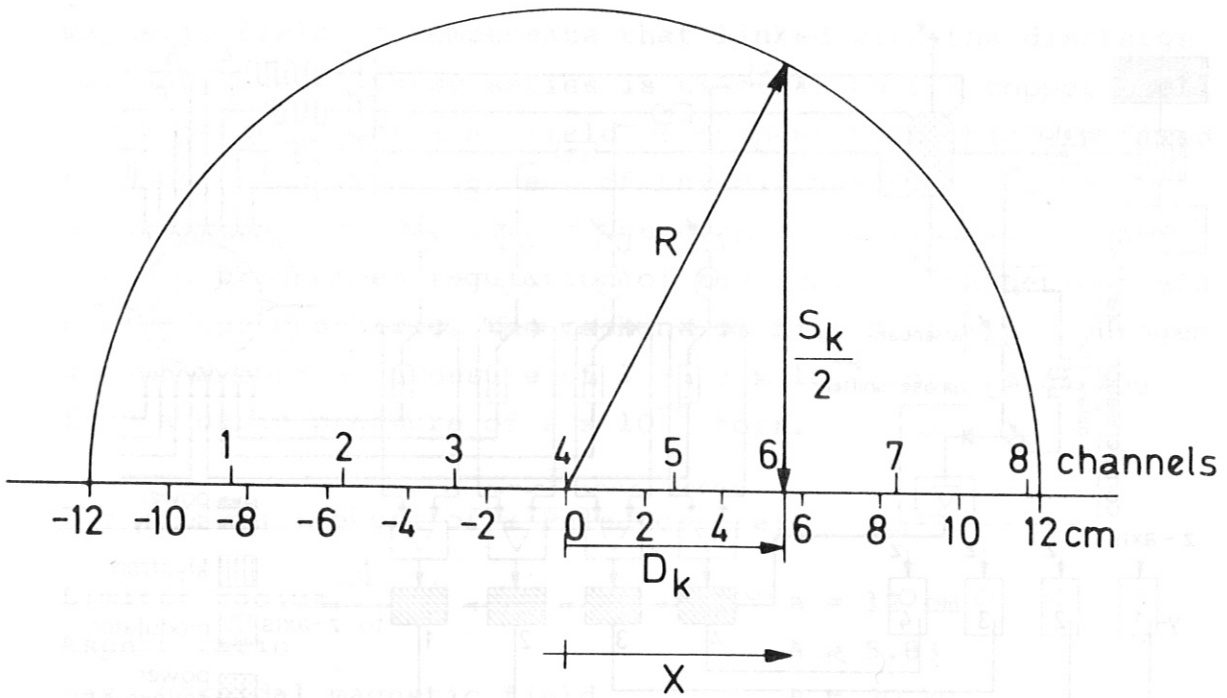(cut-off density) of the plasma.

Fig. 3 Visualisation of the path S_k for the
single interferometric channel

From (1), by measuring $\Delta\phi$ and knowing the factors before the
integral, the only information obtainable from each channel
is the value of the integral itself. Being by definition:

$$\bar{N} = \left(\int_S N(s)\,ds \right) / S \qquad (2)$$

the average density $\bar{N}$, corresponding to the path S, can thus
be obtained. Since it is not possible to know a priori the
displacement of the plasma inside the discharge tube, the
assumption is made that the paths S_k ($k = 1,2,\ldots 8$) are like
the chords of the "limiter" in correspondence with the
position of each channel.

It is then possible to write:

$$\bar{N}_k = \Delta\phi \cdot \frac{N_c}{S_k} \cdot \frac{\lambda}{\pi} \qquad (3)$$

where $S_k = 2\sqrt{R^2 - D_k^2}$, as is shown in Fig. 3. $\bar{N}_k$ is of course time dependent during the discharge pulse. Thus having measured the phase variation $\Delta\phi_k(t)$ for each channel, it will then be possible to obtain the profile of the average density $\bar{N}(x)$ for each instant of the discharge.

3) Types of Discharge

From a systematic examination of all the discharges thus far carried out at Pulsator (ca. 7000) it is possible in a first approximation to subdivide the discharges into the following three types:

a) Stable discharge with density and induced current relatively constant,

b) Instable discharge with increasing density and induced current constant,

c) Instable discharge with constant density and an increasing induced current (runaway current).

Fig. 4 a) b) shows the discharge no. 3413 which is representative of the first type (a). In Fig. 4 a) it is observed that the induced current and average density have relatively constant value throughout the whole time of the discharge. The reported average density is that of the central channel 4.

Fig. 4 b) shows the profiles of the average density of this shot at the instants of 10, 30, 50 and 70 ms; these profiles are relatively symmetrical, have an almost parabolic shape and the discharge is centred. It is a characteristic of all machines of Tokamak type that there exists the possibility of obtaining a centred discharge by means of a programmed compensating vertical magnetic field.

Fig. 5 a) shows the average density and the induced current of the shot no. 1095, representing the second type of discharge (b). From this figure one sees the almost constant value of induced current J up to the instant of instability, while the density, which since the beginning of the discharge has been of relatively high value, increases rapidly up to the point at which it presents a very rapid peak of density; the latter, as will be seen later, is characteristic of all disruptive instability of Pulsator. The density profiles for various times of the discharge no. 1095 are reported in Fig. 5 b).

They show the displacement of the discharge towards the external wall which grows with increasing density up to the instant when disruptive instability begins (34 ms). Notable still is the non-symmetric shape of the density profile which no longer presents the parabolic shape of the centred discharge previously seen. Displacement of the discharge towards the external wall and the consequent peak of density which is noticed in correspondence to the disruptive instability lead to the logical supposition that the latter should be due to a flux of particles (impurities) caused by the interaction of the discharge with the external wall. This rapid flux of impurities, so dramatically shown from the multichannel interferometry, is confirmed by the spectroscopic measurements. From Fig. 5 a) is seen that there occurs a very rapid decay in current in correspondence to the density peak. This rapid decrease in current is probably started by the impurity flux which cools the plasma. The decrease of the poloidal field associated with the current sustains in turn the instability with a decay on the discharge confinement.

The type of discharge (c) is that shown in Fig. 6 a) b) and in this can be noted an almost constant value of the density up to the instant at which the disruptive instability begins.
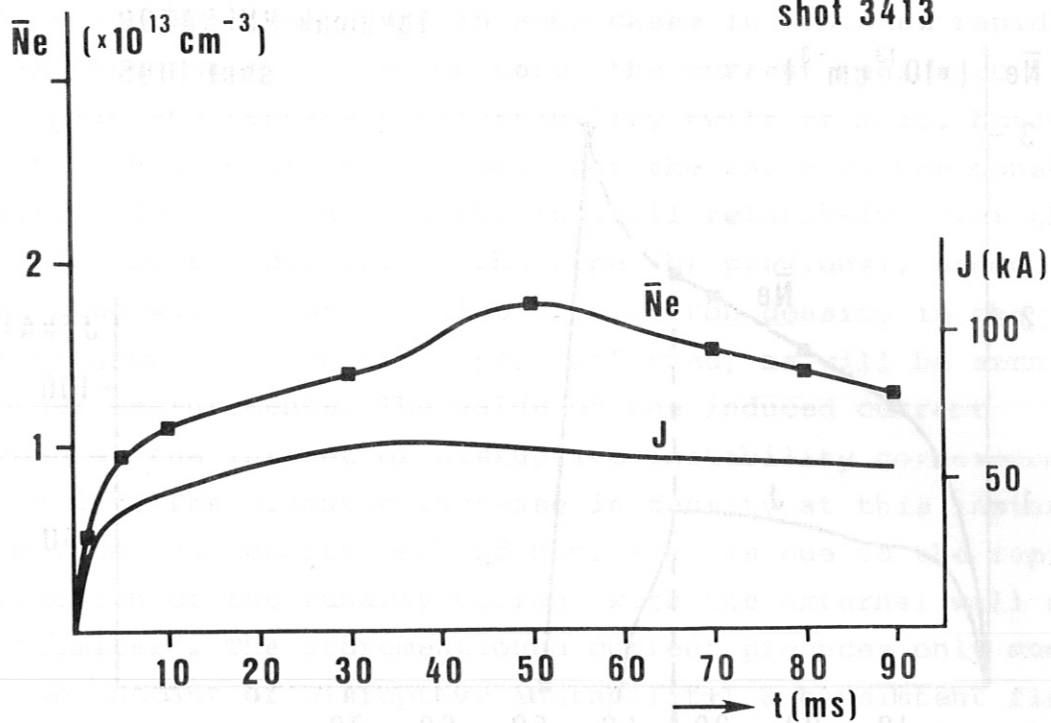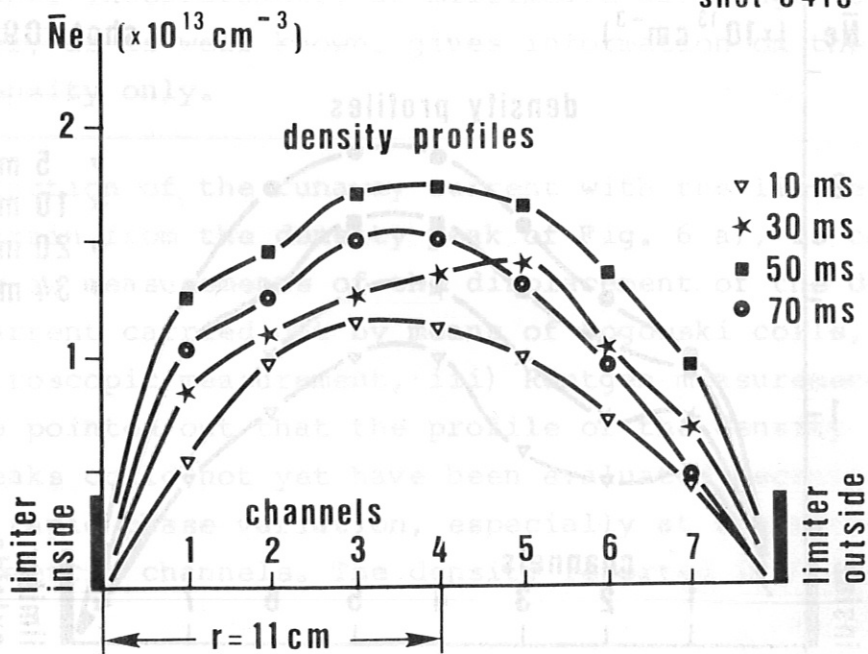
Tokamak PULSATOR
shot 3413

$\bar{N}e$ $(\times 10^{13} cm^{-3})$

$J(kA)$

$\bar{N}e$

J

t (ms)

Fig. 4 Stable discharge, a) average density $\bar{N}e$ and
induced current J

Tokamak PULSATOR
shot 3413

$\bar{N}e$ $(\times 10^{13} cm^{-3})$

density profiles

▽ 10 ms
★ 30 ms
■ 50 ms
⊙ 70 ms

limiter
inside

limiter
outside

channels

1 2 3 4 5 6 7

r = 11 cm

b) density profiles
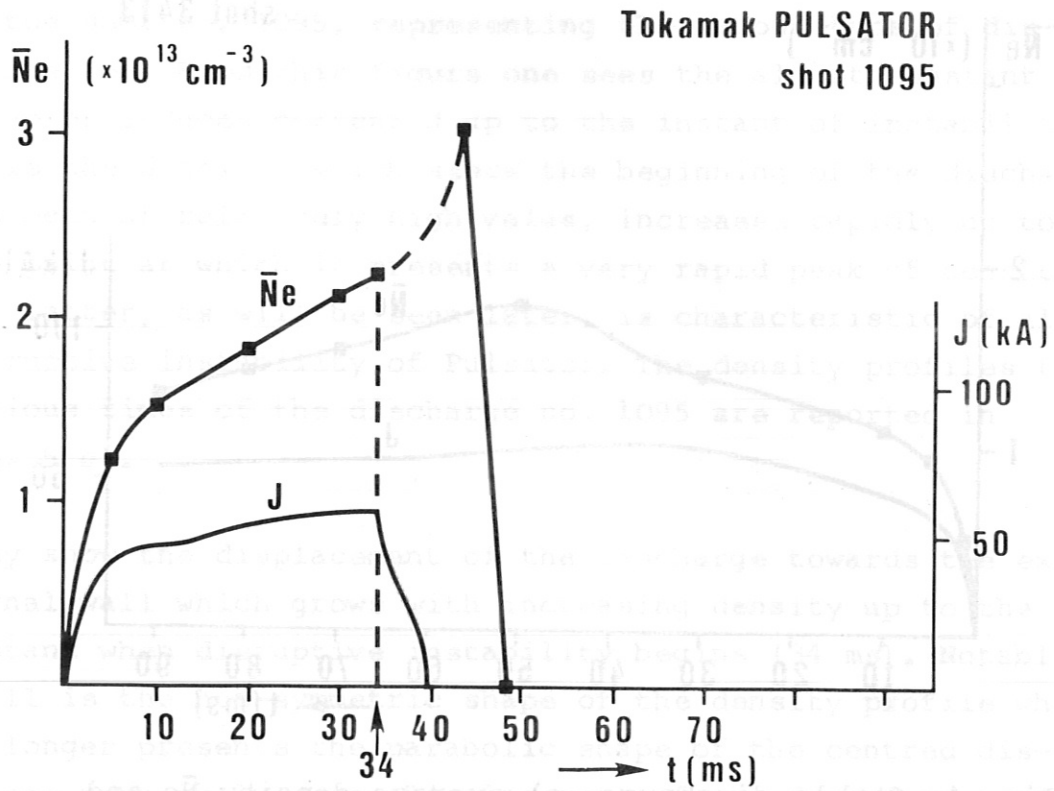
Fig. 5 Disruptive instability, a) average density $\bar{N}e$
and current J

b) density profiles
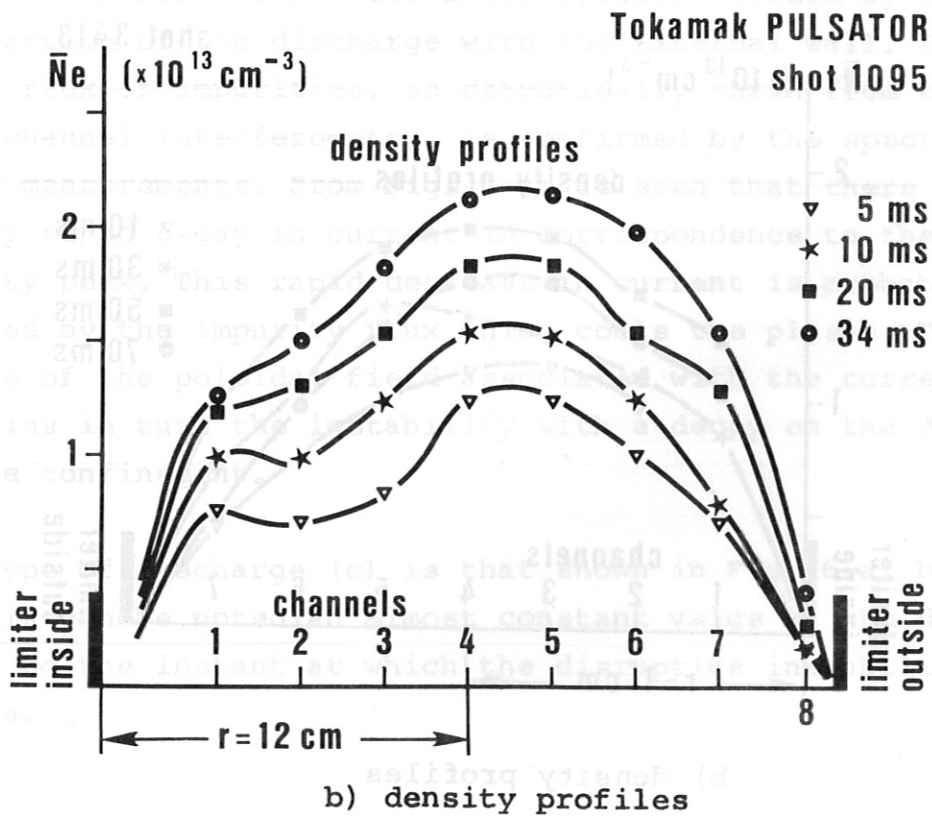
The induced current increases rapidly up to the point of disruptive instability, where in some cases it vanishes rapidly and in other cases, as shown here, the current begins to grow again and repeats the instability twice or more. Noteworthy in Fig. 6 a) is the fact that the value of the constant density before the instability is still relatively lower than the value of the density of the type (b) previously shown. Associated with this low value of electron density is the current growth of runaway type, confirmed, as will be seen by other measurements. The value of the induced current reached at the instant of disruptive instability corresponds to q = 2,7. The dramatic increase in density at this instant shown from the density peak of Fig. 6 a) is due to the rapid interaction of the runaway current with the external wall of the "limiter". The aforementioned current produces only now (at the instant of disruptive instability) a consistent flux of impurity. This is also evident from the profile of density of Fig. 6 b). Here in fact is noticed one plateau of density at the centre of the discharge tube up to the instant of the disruptive instability.

The filaments of runaway current cannot be measured from the multichannel interferometry at millimetre wavelength because the latter, as is well known, gives information on the electronic density only.

The interaction of the runaway current with the limiter wall, evident again from the density peak of Fig. 6 a), is confirmed by i) measurements of the displacement of the discharge current carried out by means of Rogowski coils, ii) spectroscopic measurement, iii) Röntgen measurement. It should be pointed out that the profile of the density relative to the peaks could not yet have been evaluated because of the very rapid phase variation, especially at the external interferometric channels. The density reported in Figs. 5 a)
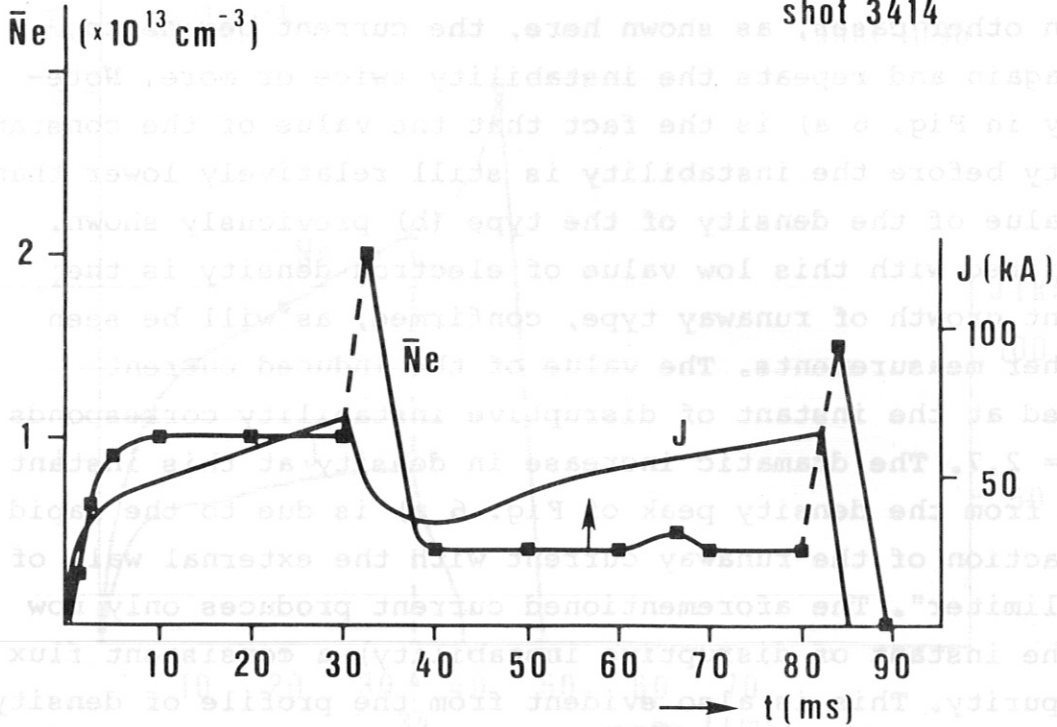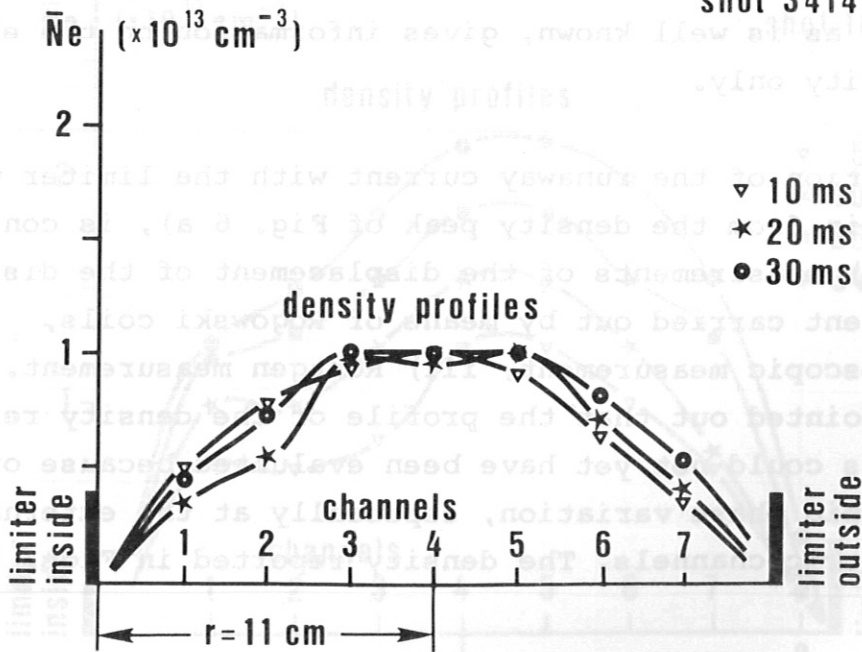
Tokamak PULSATOR
shot 3414

$\overline{N}e$ $(\times 10^{13} cm^{-3})$

J (kA)

$\overline{N}e$

J

t (ms)

Fig. 6 **Disruptive instability, a) average density** $\overline{N}e$
and current J

Tokamak PULSATOR
shot 3414

$\overline{N}e$ $(\times 10^{13} cm^{-3})$

▽ 10 ms
✶ 20 ms
● 30 ms

density profiles

limiter inside

channels

limiter outside

r = 11 cm

b) density profiles

and 6 a) is always that relative to the central channel 4, from which it has been possible to read the phase shift related to the density increase before the instability and to the density decrease after the instability; for this reason the rapid increase in density could only have been exterpolated from these measurements and is therefore indicated by a dotted line.

The reported interferometric measurements of the density profiles of a few typical discharge types only covers an elementary aspect of the Tokamak discharge. Almost everything happening to the discharge is reflected in the density measurements. The laborious elaboration of the data has so far prevented reading the density measurements in more detail. As an example, a possible explanation of the disruptive interaction of the plasma with the limiter may be the formation of magnetic islands due to MHD modes /2/. The latter reflects a fine structure on the density variation of each channel which thus far has not yet been evaluated.

II BASIC CONSIDERATIONS

1) The Measurement of Average Density

Let us consider an electromagnetic wave

$$u = U e^{j\gamma(x,t)}$$

where $\gamma(x,t) = \omega t \pm kx$ is the phase angle of the wave and $k = (\omega/c)n$ is the wave number of the wave radiating in a medium of refraction index n.

In vacuum $n_o = 1$ and consequently $k_o = 2\pi / \lambda_o$ where λ_o is the wavelength in the vacuum. For any medium $n = \lambda_o / \lambda$ is valid.

By considering an ordinary wave propagating through a plasma, the following dispersion relation is valid:

$$\varepsilon = n^2 = 1 - \frac{(\omega_p / \omega)^2}{1 - j(\nu / \omega)} \qquad (4)$$

where $\omega_p^2 = Ne^2 / m_e \varepsilon_o$ is the plasma frequency; ω is the frequency of incident wave to which one can associate a cut-off density N_c given by

$$\omega^2 = N_c e^2 / m_e \varepsilon_o$$

and ν is the collision frequency.

For a non-collisional plasma $\nu \approx 0$, hence we have

$$n^2 = 1 - (\omega_p / \omega)^2$$

or by introducing the density

$$n^2 = 1 - N / N_c \qquad (5)$$

To evaluate the electron density of a plasma one uses the measurement of the phase variation $\Delta\phi$ which affects one wave travelling through the plasma. $\Delta\phi$ can be expressed by:

$$\Delta\phi = \int_s [k_o - k(s)] \, ds = k_o \int [1 - n(s)] \, ds \qquad (6)$$

where the integral is extended over the path of the wave into the plasma.

By substituting Eq. 5 into Eq. 6 is obtained:

$$\Delta\Phi = k_0 \int_S [1 - (1 - N/N_c)^{\frac{1}{2}}] \, ds \qquad (7)$$

For $N/N_c \ll 1$ one has in good approximation

$$(1 - N/N_c)^{\frac{1}{2}} \simeq 1 - 1/2 \, (N/N_c)$$

from which, substituting into Eq. 7, one obtains:

$$\Delta\Phi = \frac{k_0}{2 N_c} \int_S N(s) \, ds = \frac{\pi}{\lambda_0 N_c} \int_S N(s) \, ds \qquad (8)$$

Without considering refraction phenomena i.e. by assuming a straight path S_k of the wave into the plasma (c.f. Fig. 3) and indicating with

$$\bar{N}_k = \int_0^{S_k} [N(s)/S_k] \, ds \qquad (9)$$

the average density relative to the path S_k of each channel $k = 1,2,\dots 8$ in the interferometric system previously seen, one obtains:

$$\Delta\Phi_k = \frac{\pi \, \bar{N}_k \, S_k}{\lambda_0 \, N_c} \qquad (10)$$

From this has been derived Eq. 3, previously employed for the determination of the average density profiles $\bar{N}(x)$.

2) The Problem of Abel Inversion

The problem of Abel inversion consists in the transformation
of the profile of average density into the profile of local
density. This transformation is only possible if the profile
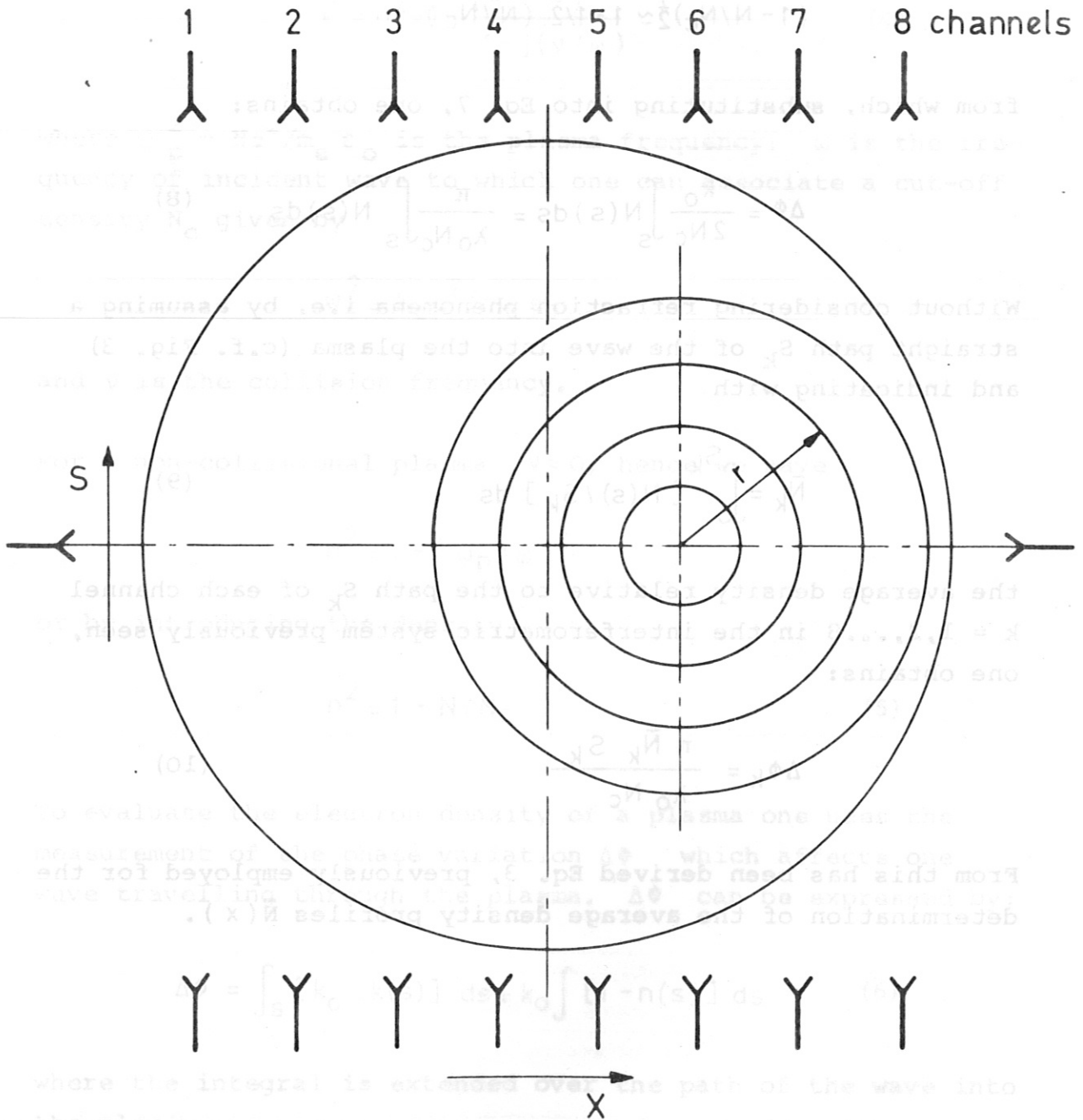of average density is symmetrical.

Fig. 7 Visualisation of the radial symmetry assumed
for an analytical Abel's transformation

Assuming a radial symmetry of density $N(r)$ as shown for example in Fig. 7, one can, from each point data $\Delta\phi_k$ of Eq. 10 obtain the profile $\phi(x)$ which, with the coordinate of Fig. 7, can be expressed by:

$$\phi(x) = \frac{1}{2} \frac{\omega}{cN_c} \int_x^R \frac{N(r)\, r\, dr}{\sqrt{r^2 - x^2}} \qquad (11)$$

By applying an Abelian transformation it would then be possible to obtain the density expressed by:

$$N(r) = -N_c \frac{2c}{\pi\,\omega} \int_r^R \frac{\phi'(x)\, dx}{\sqrt{x^2 - r^2}} \qquad (12)$$

However this analytical transformation is difficult to apply due to the error caused by the extrapolation of the phase-shift profile $\phi(x)$ from the single phase-shift data $\Delta\phi_k$ averaged by each channel k with the assumption of the path length S_k of the wave into the plasma, as shown by Fig. 3. The error will be increased still more in passing to the value of the derivative $\phi'(x)$, which appears in the integral of Eq. 12.

On the other hand, in the study of the discharge of Pulsator, as already seen, we generally find non-symmetrical profiles of plasma density.

It is then necessary to apply known grafical or numerical methods, /3/, /4/, /5/, /6/, of much greater validity, but one should make a priori some assumptions on the qualitative shape of the local plasma density distribution which is still to be evaluated.

In order to be able to work out the density distribution of non-symmetrical type without the use of other not directly related experimental data (e.g. without using the data relative

to the radial shift of current, as would be necessary in the case of Fig. 7), a more convenient grafical-numerical method of simple application has been recently proposed /7/. This method is illustrated in Fig. 8, where the profile of local density is evaluated from the profile of average density relative to the Pulsator discharge no. 1110 at t = 50 ms.
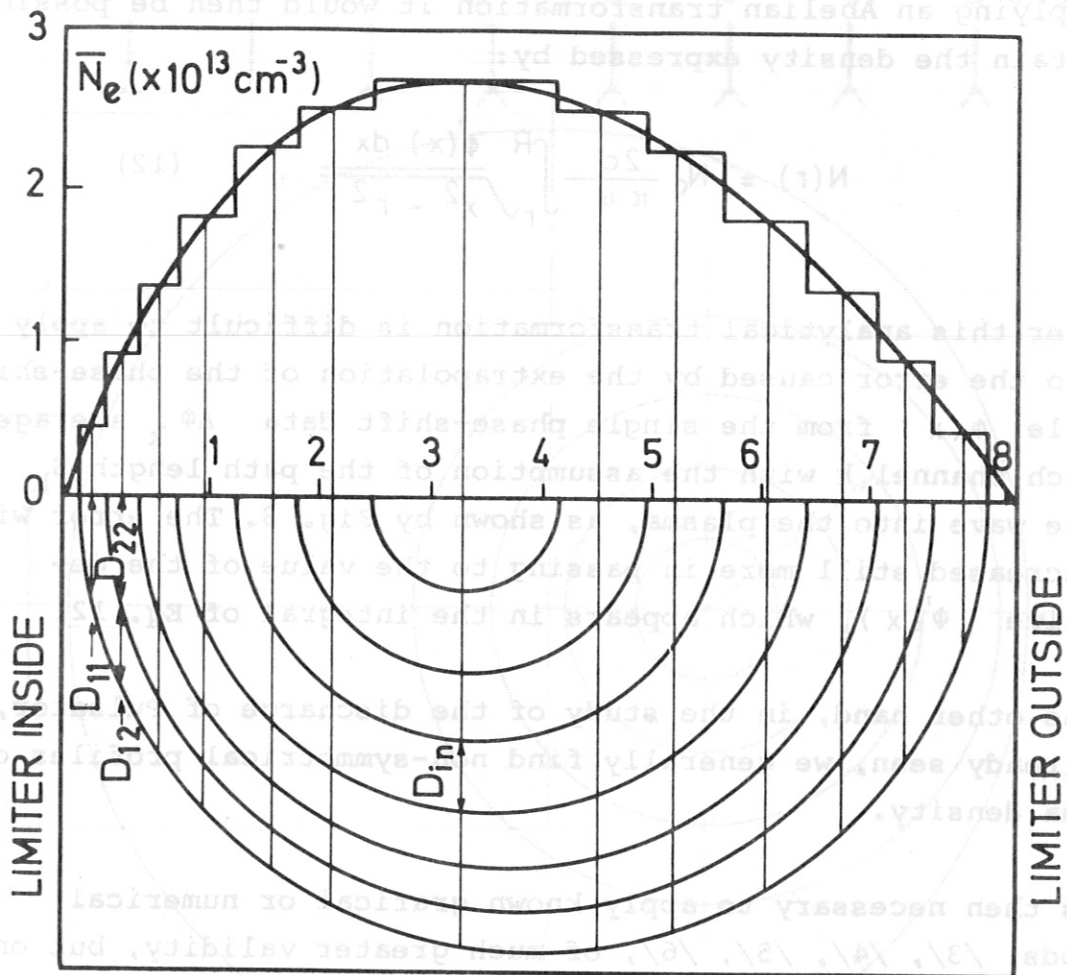

Fig. 8 a) Average density distribution $\bar{N}$ and relative numerical-grafical transformation

As shown in Fig. 8 a) the profile of average density is approximated with a step function of density.
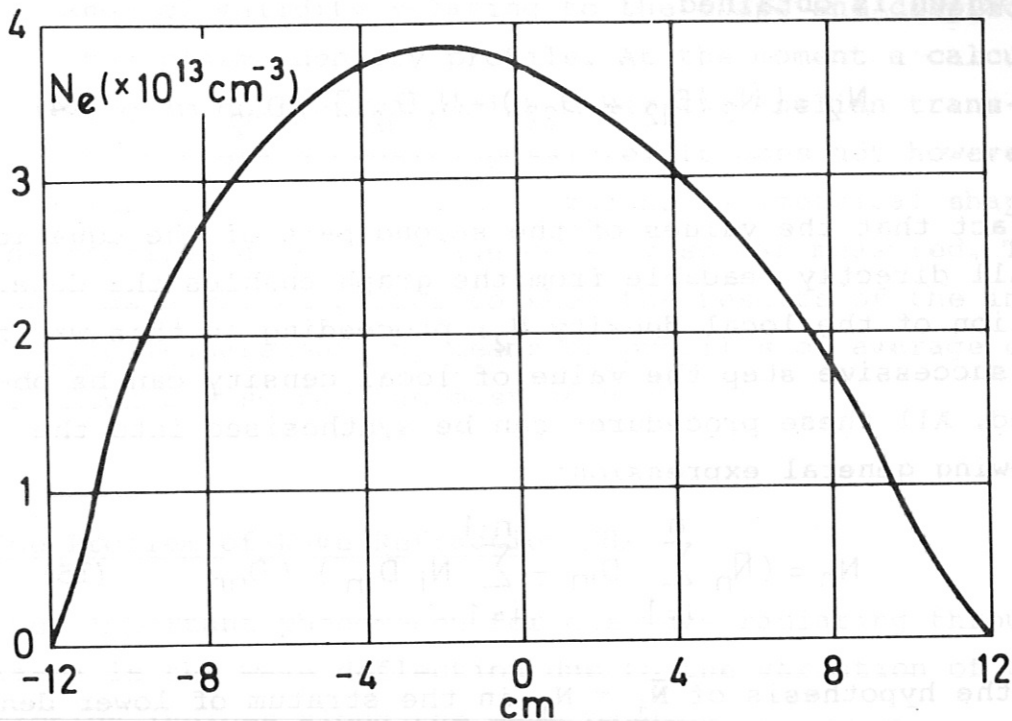
Fig. 8 b) Transformed local density distribution

Assuming that the density of the plasma is symmetrical with
respect to the equatorial plane of the toroidal discharge
tube, we also assume that the line of constant density
consists, as is shown in Fig. 8 a), of circles, generally
non-concentric.

In Fig. 8 the circles of constant density corresponding to
the various step values $\bar{N}_n$ of the average density profile
are constructed. It is now possible to determine the path D_{in},
through strata of different average density, of hypothetical
beams of electromagnetic waves passing through the inter-
section points of the density curve with the single steps
of density.

Assuming that the average density $\bar{N}_1$ would be equal to the
local density N_1 it can be written that

$$\bar{N}_2 (D_{12} + D_{22}) = N_2 D_{22} + N_1 D_{12} \qquad (13)$$

from which is obtained

$$N_2 = [\bar{N}_2 (D_{12} + D_{22}) - N_1 D_{12}] / D_{22} \qquad (14)$$

The fact that the values of the second part of the equation are all directly readable from the graph enables the determination of the local density N_2; proceeding in this way for each successive step the value of local density can be obtained. All these procedures can be synthesised into the following general expression:

$$N_n = (\bar{N}_n \sum_{i=1}^{n} D_{in} - \sum_{i=1}^{n-1} N_i D_{in}) / D_{nn} \qquad (15)$$

With the hypothesis of $\bar{N}_1 = N_1$ in the stratum of lower density, (first step of density), one can best identify the local density with the average density because the hypothetical beam of microwaves radiating through only one single stratum is excluding all density gradient due to the other density strata. These grafical-numerical procedures, applied to the seven density steps in Fig. 8 a) have enabled the distribution of local density shown in Fig. 8 b) to be obtained.

In other words this procedure changes the density steps of Fig. 8 a), corresponding to the average value of the density obtained from the phase shift data of the single channels, into the maximum value of density supposed at the geometrical centre of the plasma path of the single channels.

This original method of Abel inversion, applicable to non-symmetrical profiles of density, is nevertheless manually very laborious. For this reason the translation of this system into a calculation program is being developed. In the future this will enable an immediate transformation of the Abelian type of the multichannel interferometer data with a

large range of validity relating to the shape and displace-
ment of the plasma density profile. At the moment a calcu-
lation program does exist, which makes the Abelian trans-
formation of average density possible. It does not however
give satisfactory results due to the non-symmetrical shape
of the profiles of the average density so far measured. This
is the reason why we prefer to show the results of the inter-
ferometric measurements by means of profiles of average den-
sity, which are so far the most accurate.

3) The Problem of Wave Refraction /8/

Another important phenomenon for one wave radiating through
a plasma is the wave deflection due to the variation of the
refraction indices along the wave path.

Let us consider a cylindrically symmetric plasma whose elec-
tron density N is a slowly varying, monotomically decreasing
function of radius r. From Fig. 9 the differential equation
satisfied by the ray path $r(\theta)$ in a cylindrically stratis-
fied medium can be readily obtained from Snell's law. If the
refraction index n is a function of r, then Snell's law takes
the form:

$$n(r) \cdot r \cdot \sin \alpha = \text{constant} \qquad (16)$$

where α is the angle between the ray and the radial direction.

From the triangle PP'Q of Fig. 9 we see that:

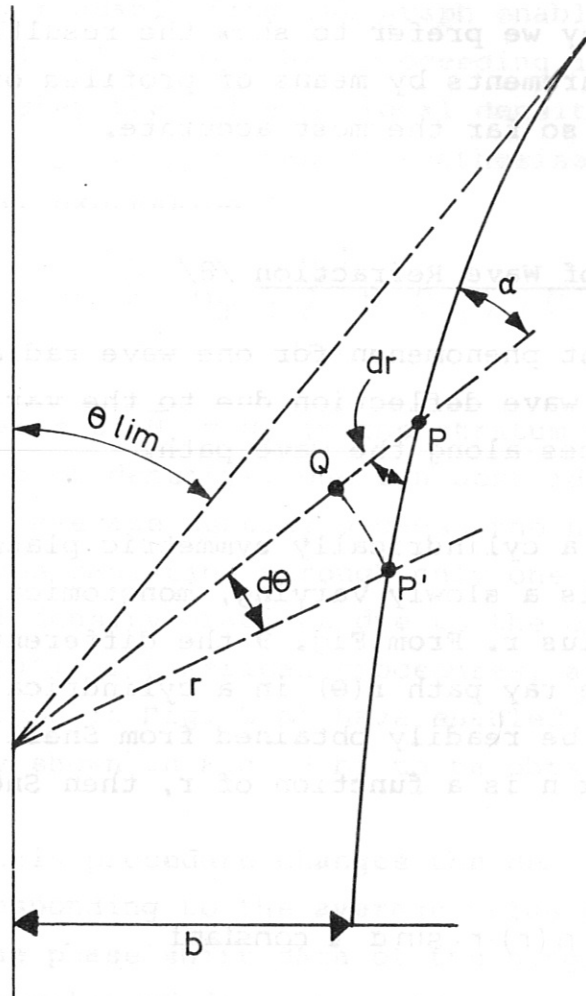$$r \, d\theta / dr = tg \, \alpha \qquad (17)$$

Fig. 9   Ray path

Eliminating α between Eq. 16 and 17 and with various elaborations, is obtained the deflection angle of the ray, i.e. the limiting value θ_{lim} of the angular coordinate as $r \longrightarrow \infty$. As a function of the impact parameter b the deflection angle of the ray is expressed by:

$$\theta_{lim}(b) = \pi - 2 \int_{r_o}^{\infty} r^{-2} \left[b^{-2} - r^{-2} - b^{-2} V(r) \right]^{-1/2} dr \qquad (18)$$

where r_o is the distance of closest approach for this ray
i.e. $d\theta/dr = \infty$ in Eq. 17 and $V(r) = N(r)/Nc$. /8/

Assuming a parabolic distribution of density expressed by:

$$V(r) = V_0 \left[1 - \left(\frac{r}{a}\right)^2 \right]$$

(valid for $r < a$ and where $V_0 = N_0/Nc$ is the maximum value
of the parabola and a being the plasma radius) one obtains:

$$\theta_{lim}(b) = \sin^{-1} \frac{V_0 \left[\left(\frac{b}{a}\right)^2 - \left(\frac{b^4}{a}\right) \right]^{1/2}}{\left\{ V_0 \left(\frac{b}{a}\right)^2 + \left[\left(\frac{1-V_0}{2}\right) \right]^2 \right\}^{1/2}} \tag{19}$$

By looking at this function it can be seen that the deflection
angle varies from a O value for $b = O$ through a maximum value
returning to O for $b = a$. This maximum angle of deviation of
the wave can be expressed with good approximation in (rad) by:

$$\theta_{max} = \sin^{-1} \frac{N_0}{N_c} = \sin^{-1} \left[8,96.10^{-16} N_0 \lambda^2 \right] \tag{20}$$

where the density is expressed in cm^{-3}, λ in mm.

4) Frequency Selection

Equation 20 is very convenient for calculating the deviation
of the ray path at the receiver antenna

$$d \approx 2a\theta_{max} \tag{21}$$

As an example Table 1 shows for three different wavelengths
$\lambda = 2$, 1 and 0,337 mm: i) the phase shift expressed in fringe
number $\Delta\phi / 2\pi$ given by Eq. 10; ii) the maximum angle of de-
viation θ_{max} given by Eq. 20 and iii) the deviation d of the
ray path at the receiver antenna given by Eq. 21 for the two
IPP Tokamaks, ASDEX and PULSATOR. The calculations are shown
for two maximum values of density assuming a parabolic density
distribution. Looking at Table 1 we can make the following
statements regarding the working frequency for ASDEX:

First of all we have, as will be shown later, excellent results
at the working wavelength of $\lambda = 2$ mm for Pulsator.

These results are valid up to the thus far measured maximum
density value of $N_e \simeq 6 \div 8 \cdot 10^{13}$ cm^{-3}. This means that in
Pulsator we have been working with a maximum deviation of
$d \simeq 5 \div 7$ cm at the receiver.
Hence for ASDEX one could expect a fairly good density distri-
bution measurment at a $\lambda = 2$ mm, up to a maximum density
value of $2 \div 3 \cdot 10^{13}$ cm^{-3}.

It is noteworthy that the maximum angle of deviation of the
ray path occurs somewhere between the centre of the discharge
and the plasma edge. Thus only two, or in extreme cases for
even larger density only four of twelve channels will be
affected by refraction problems. On the other hand, ASDEX
being a machine primarily designed to test the feasibility of
a magnetic limiter, security considerations may limit the
maximum value of the density at $Ne \simeq 5 \cdot 10^{13}$ cm^{-3} for the
largest part of the experiments. In this case the afore-
mentioned considerations predict that the use of probing beams
at $\lambda = 2$ mm is appropriate.

The wavelength at $\lambda = 1$ mm, although seeming ideally suited
for the ASDEX density distribution measurements, will not be
considered because of the low power and high cost of the
available sources.

Of course, as will be seen later in detail, the development of the Laser-submillimetre wave at $\lambda = 0,337$ mm should be vigorously sustained in order to reach the reliability and simple installation requirements as at $\lambda = 2$ mm.

Table I

Choice of Frequency

- ASDEX - Ne = 3×10^{13} cm^{-3}, R = 40 cm

λ (mm)	Number of Fringes	Maximum deflection angle (rad)	Maximum deviation at the receiver (cm)
2	14,4	12 x 10^{-2}	9,6
1	7,2	3 x 10^{-2}	2,4
0,337	2,5	0,34 x 10^{-2}	0,27

- ASDEX - Ne = 10^{13} cm^{-3}, R = 40 cm

2	4,8	4 x 10^{-2}	3,2
1	2,4	1 x 10^{-2}	0,8
0,337	0,8	0,11 x 10^{-2}	0,09

- PULSATOR - Ne = 3×10^{13} cm^{-3}, R = 11 cm

2	4	12 x 10^{-2}	2,6
1	1,9	3 x 10^{-2}	0,7
0,337	0,6	0,34 x 10^{-2}	0,07

III MULTICHANNEL INTERFEROMETRY

By radiating the plasma with several beams of electromagnetic
waves, each beam furnishes a point data for the density pro-
file. It is advantageous to have as many radiating channels
as possible in order to evaluate the density profile with a
satisfactory number of details. This tendency is contrastated
by several technical difficulties, the most important being
the beam divergence for the millimetric waves and the beam
width for the Laser-submillimetric waves. In order to avoid
information from one channel being detected by other channels,
it is then necessary to have some means of beam selection.
Heterodyne selection, besides being expensive, is faced with
problems of frequency stability. Instead, serrodyn frequency
shift in millimetric waves and Doppler frequency shift in sub-
millimetric waves is the alternative solution thus far used.
In the following, both frequency shift methods with their
interferometric detection systems will be illustrated.

1) Linear Detection

Before discussing the interferometric circuitry, let us look
at the basic rules for obtaining a linear detection of the
phase shift $\Delta\Phi$ experienced by a wave in probing the plasma.
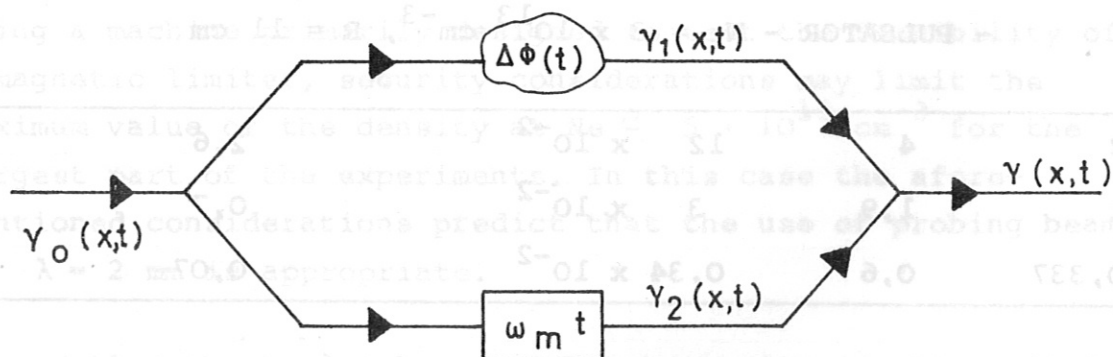
Fig. 10 Schematic of the detection circuitry

With reference to Fig. 10 a wave $u_o = U_o e^{j\gamma_o(x,t)}$ (where $\gamma_o(x,t) = \omega_o t + k_o x$ is the time and space dependent phase angle) is divided into two waves, one of which, labelled in Fig. 10 as:

$$u_1 = U_1 e^{j\gamma_1(x,t)} \tag{22}$$

is radiated through the plasma and the other

$$u_2 = U_2 e^{j\gamma_2(x,t)} \tag{23}$$

is used as a reference wave.

The wave radiated through the plasma experiences a phase shift $\Delta\Phi$ given by Eq. 10, which is in general time dependent, hence the phase angle γ_1 may be expressed by:

$$\gamma_1(x,t) = \gamma_o(x,t) + \Delta\Phi(t) \tag{24}$$

The previously mentioned frequency shift of the carrier wave from ω_o to $\omega_o + \omega_m$, which will be discussed in detail later, may be inserted either in the measuring or in the reference branch; in Fig. 10 it has been inserted into the reference branch, hence the phase angle γ_2 can be expressed by:

$$\gamma_2(x,t) = \gamma_o(x,t) + \omega_m t \tag{25}$$

By superimposing the two signals of Eq. 22 and 23 we obtain

$$u = u_1 + u_2 = U_o e^{j\gamma(x,t)} \tag{26}$$

Neglecting at the superimposition point the space dependence of the phase angle, Fig. 11 shows that:

$$U = \left\{ U_1^2 + U_2^2 + 2 \cdot U_1 U_2 \cos\left[\gamma_2(t) - \gamma_1(t) \right] \right\}^{1/2} \tag{27}$$

and $\qquad \gamma(t) = \gamma_1(t) + \psi(t)$

where

$$\psi(t) = \text{arc tan} \frac{U_2 \sin [\gamma_2(t) - \gamma_1(t)]}{U_1 + U_2 \cos [\gamma_2(t) - \gamma_1(t)]} \qquad (28)$$
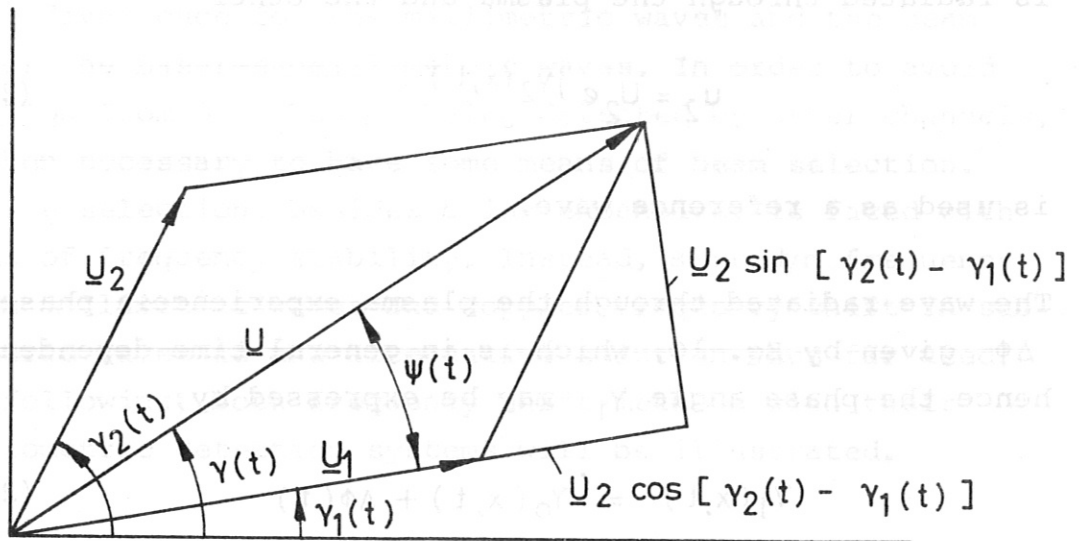
Fig. 11 Grafic illustration of Equation 27

On rectifying with a square-law crystal diode the low-frequency component of the rectified signal is

$$u \propto \left\{ U_1^2 + U_2^2 + 2U_1 U_2 \cos [\gamma_2(t) - \gamma_1(t)] \right\} \qquad (29)$$

From Eq. 24 and 25 we obtain:

$$\gamma_2(t) - \gamma_1(t) = \omega_m t - \Delta\Phi(t)$$

The ac component of Eq. 29:

$$u \propto U_1 U_2 \cos [\omega_m t - \Delta\Phi(t)] \qquad (30)$$

is filtered up by means of a tuned amplifier. Equation 30 can be regarded as an intermediate frequency ω_m, the amplitude of which is proportional to the amplitude U_1 of the measuring carrier signal (for constant amplitude of the reference signal) and the phase of which $\Delta\Phi(t)$ is that experienced by the carrier wave on probing the plasma. The phase modulation $\Psi(t)$ of Eq. 28 for the carrier frequency is not important, because only the amplitude variation is detected.

The linear detection expressed by Eq. 30, which is valid for the square-law part of the silicon diode characteristic, holds for low power levels up to a few milliwatts. For power levels beyond the square-law range, the useful signal is subjected to distortion.

Linear detection can however be re-established as in all heterodyne systems if the level of the received signal is lower, almost 20 dB, than that of the reference signal.

This is seen by re-writing Eq. 27:

$$u \approx U_2 \left\{ 1 + \frac{U_1^2}{U_2^2} + 2\,\frac{U_1}{U_2} \cos\left[\omega_m t + \Delta\Phi(t)\right] \right\}^{1/2}$$

With $\dfrac{U_1}{U_2} \ll 1$ and neglecting the quadratic term we obtain:

$$u \approx U_2 + U_1 \cos\left[\omega_m t + \Delta\Phi(t)\right] \tag{31}$$

As shown in Fig. 12, the amplitude variation of the reference signal U_2 due to the superimposition of the probing signal U_1, as expressed by Eq. 31, is equivalent to single-side band modulation.

In Fig. 12 the phase modulation Ψ for the carrier frequency expressed by Eq. 28 is of no significance at all for the low frequency useful signal.
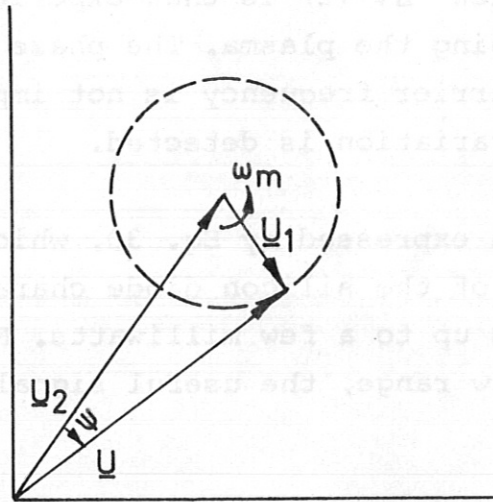
Fig. 12 Grafic illustration of Equation 31

2) Frequency Shift

Referring to Fig. 10, from the phase angle of the carrier wave

$$\gamma_0(x,t) = \omega_0 t + kx \qquad (32)$$

we have the possibility of shifting the frequency ω_0 of the carrier wave by a small amount ω_m, either by varying k or by varying x in function of the time in such a way that either is

$$\frac{x\,dk(t)}{dt} = \omega_m \qquad (33)$$

or

$$k\,\frac{dx(t)}{dt} = \omega_m \qquad (34)$$

One can easily vary $k(t) = \frac{2\pi}{c} f(t)$ in millimetric wave sources such as klystrons or carcinotrons by frequency modulation. Instead, in submillimetric wave sources as for example HCN-Laser, it is more convenient to vary x by a small amount, i.e. one wavelength, thus obtaining the frequency shift by Doppler effect.

In the following we show the derivation of the frequency shift in both cases:

a) <u>Frequency modulation</u> /9/ /10/ /11/ /12/ /13/ /14/
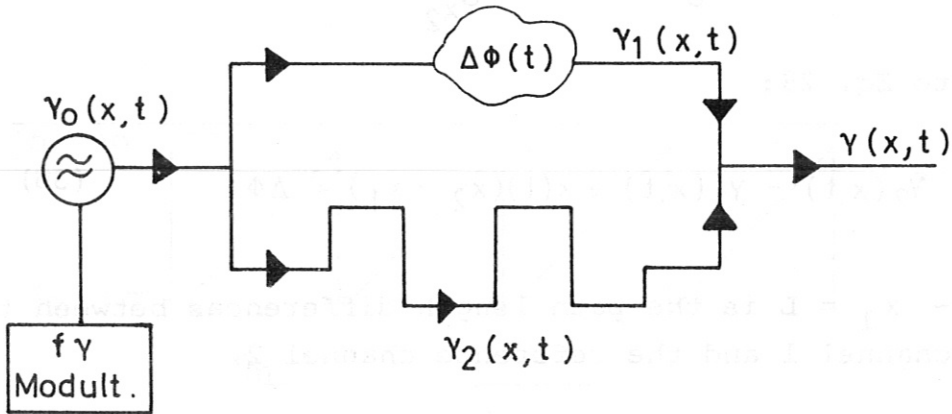
Fig. 13   Schematic of the interferometer with
          frequency modulation

To obtain Eq. 33 from $k(t) = \frac{2\pi}{c} f(t)$ we only need to vary the carrier frequency in such a way that:

$$f(t) = f_0 + \Delta f \frac{t}{T_m} \qquad (35)$$

as visualised in Fig. 14
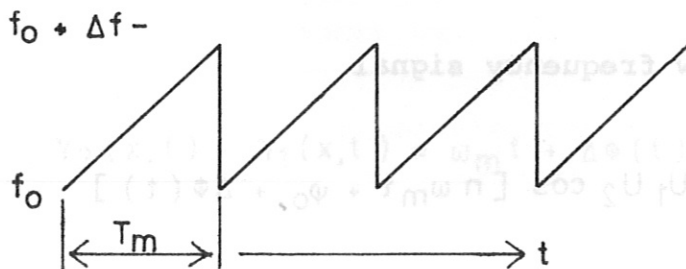
Fig. 14   Visualisation of Equation 35

We should note that in Eq. 32 we have to take into account the frequency deviation of the carrier wave ω_o by writing:

$$\gamma_0(x,t) = 2\pi \int f(t)\,dt + k(t) \int dx \qquad (36)$$

Thus we can also write (c.f. Fig. 13):

$$\gamma_1(x,t) = 2\pi \int f(t)\,dt + k(t) \int_{x_1} dx + \Delta\phi(t) \qquad (37)$$

$$\gamma_2(x,t) = 2\pi \int f(t)\,dt + k(t) \int_{x_2} dx$$

Referring to Eq. 29:

$$\gamma_2(x,t) - \gamma_1(x,t) = k(t)(x_2 - x_1) + \Delta\phi\,t \qquad (38)$$

where $x_2 - x_1 = L$ is the path length differences between the measuring channel 1 and the reference channel 2.

As we shall see, this path difference can be chosen at will by using retarding lines.

Substituting Eq. 35 into Eq. 38 we obtain:

$$\gamma_2(x,t) - \gamma_1(x,t) = \frac{\Delta f \cdot L}{c}\,\omega_m t + \frac{2\pi L}{\lambda_o} + \Delta\phi(t) \qquad (39)$$

and by choosing Δf or L in order that

$$\frac{\Delta f \cdot L}{c} = n = 1;\ 2;\ 3;\ \ldots\ldots \qquad (40)$$

we obtain the low frequency signal

$$u \propto U_1 U_2 \cos\left[n\,\omega_m t + \varphi_o + \Delta\phi(t)\right]$$

as previously seen in Eq. 30 and Eq. 31.

b) <u>Doppler frequency shift</u>

Referring to Fig. 10 let us write again the phase angle of the measuring wave

$$\gamma_1(x,t) = \gamma_0(x,t) + \Delta\phi(t)$$

To shift the frequency in the reference channel we vary the path length x , as stated by Eq. 34, thus having

$$\gamma_2(x,t) = \omega_0 t + k_0 x(t) \tag{41}$$
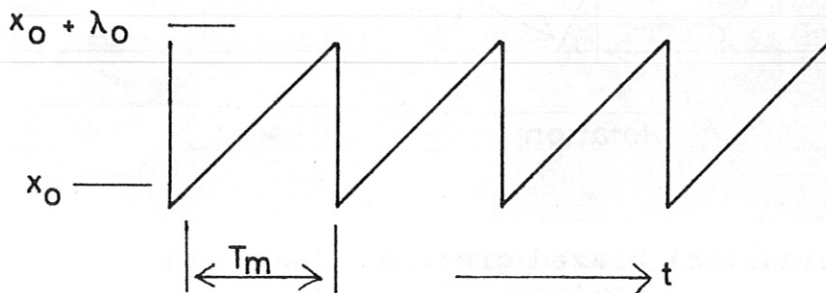
Fig. 15 Visualisation of Equation 42

As shown in Fig. 15 is:

$$x(t) = x_0 + \lambda_0 \frac{t}{T_m} \tag{42}$$

Substituting into Eq. 41

$$\gamma_2(x,t) = \gamma_0(x,t) + \omega_m t$$

and being

$$\gamma_2(x,t) - \gamma_1(x,t) = \omega_m t + \Delta\phi(t)$$

the low frequency signal is again:

$$u \propto U_1 \, U_2 \cos \left[\omega_m t + \Delta\phi(t) \right] \qquad (43)$$

as previously seen in Eq. 30.
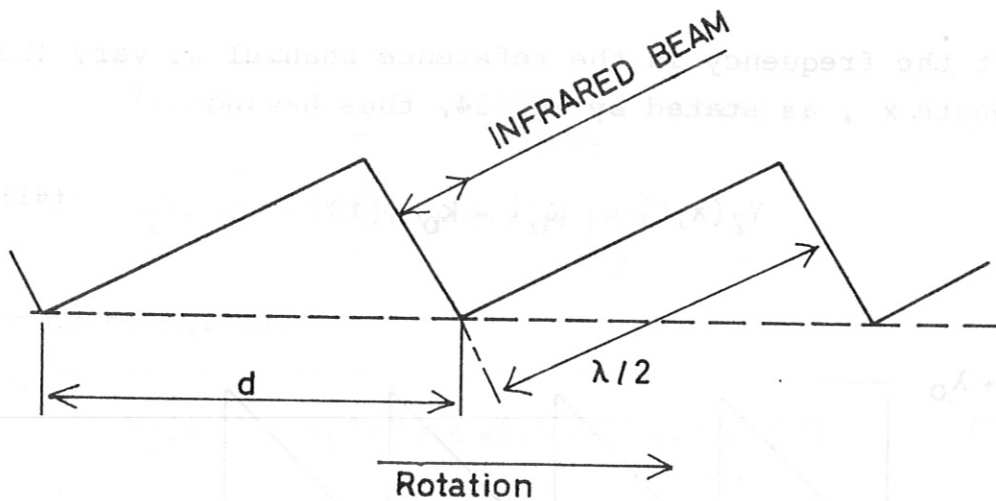
Fig. 16   Cylindrical blazed grating

The path length variation $x(t)$ producing the frequency shift ω_m has been realised by VERON /15/ /16/ by diffracting a 337 µm Laser beam off a rotating grating. The cylindrical grating is of blazed type with grooves parallel to its axis (c.f. Fig. 16). By denoting with R the radius of the cylinder, with N its rotational speed in revolutions per second and with $G = 2\pi R/d$ the total number of grooves on the grating, the frequency shift will be:

$$f_m = G \cdot N \qquad (44)$$

This frequency lies on the same range (from 10 kHz to 500 kHz) as that obtained with the use of retarding lines by the frequency modulation of the millimetre wave sources.

3) Interferometer Circuitry

In the millimetre wave range, the availability of highly de-
veloped components such as high power sources, sensitive de-
tectors, directional couplers, hybrid junctions etc, allows
a rugged assembling of such a complex system of a multichannel
interferometer as that shown schematically in Fig. 2.
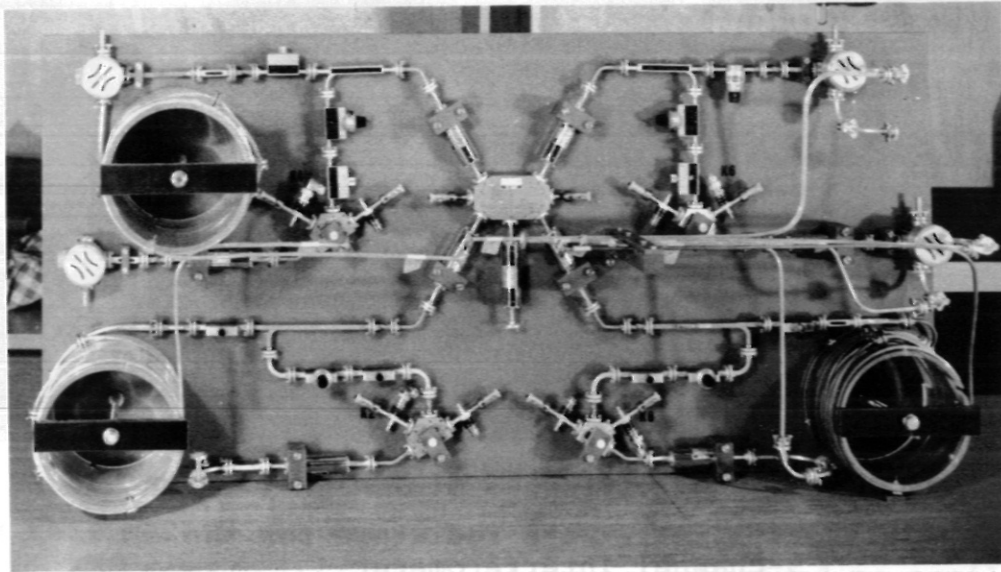
Fig. 17   Panel assembling for 4 channels
of the interferometers

Fig. 17 shows such assembling in "panels" form for almost all
millimetre wave components of the four channels shown in Fig. 2.
The small dimensions of the used waveguide RG98U for $\lambda = 3,3$ mm
and RG136U for $\lambda = 2$ mm allow a simple construction of the
retarding waveguide length "L" of Eq. 40 used to achieve the
detector selection $n \omega_m$ of the single channels of the inter-
ferometers.

The very rugged assembling for all the 18 radiators of the 9-
channel interferometer is shown in Fig. 18.
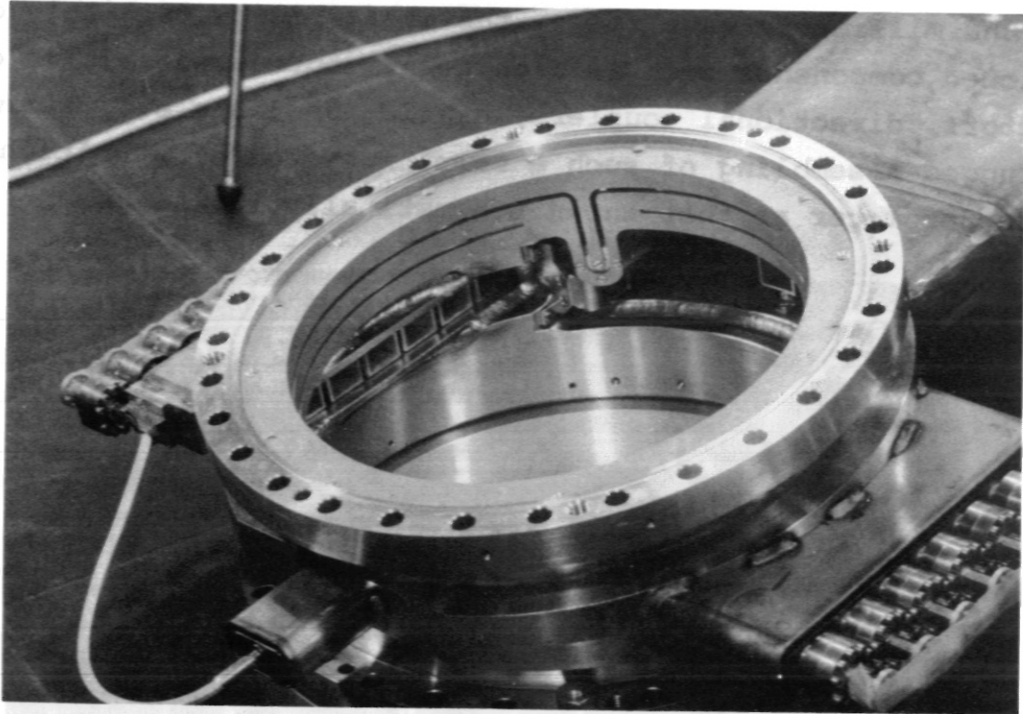
Fig. 18   Millimetre wave radiators for the
9-channel interferometer

In general, despite its complexity, the multichannel inter-
ferometer in millimetre wavelength can be assembled in a very
compact form, in a small volume, and has a high degree of
reliability.

The construction of the submillimetre Laser interferometer has
been on the other hand up to now limited to a single channel
at the Tokamak TFR of Paris /16/.

For the extension of this interferometer to a system of several
channels there are some difficulties due to the large volume
and low-power output of the sources, large beam diameter low
detection sensitivity, and complexity of the channel selection.

In the following, after describing the millimetre multichannel
interferometers and the submillimetre Laser interferometer,
we conclude this report with some suggestion on the further
development of these diagnostic techniques.

a) Multichannel millimetre-wave interferometer

The method of frequency modulation, first used by C.B. WHARTON
/9/ to measure plasma density by means of fringe-shift display,
has been modified in 1960 by G. LISITANO /13/ to satisfy the
simple condition $\Delta f \cdot L/c = 1$ expressed by Eq. 40. The fre-
quency deviation Δf set is of the order of 10 Mc/s, which is
very small compared with a fundamental frequency f_o at 90 Gc/s
and over. Since the modulating frequency f_m (of the order of
100 kc/s to 500 kc/s) is also very low, the side band amplitudes
of the frequency-modulated wave decrease very rapidly. The
frequency-modulated oscillation may thus be regarded virtually
as a purely spectral line. In this respect it is possible, by
using this method to reduce any frequency to any lower inter-
mediate frequency without resorting to a heterodyne oscillator.
The phase detection is readily achieved because the inter-
ference signal has the same frequency as the modulating saw-
tooth voltage.

This method has been applied in Tokamak T-3 by E.P. GORBUNOV
/3/ in order to obtain the low frequency selection of several
interferometric channels used to measure the spatial electron-
density distribution during the discharge.

All channels are supplied at the same high frequency in the
millimetric wave range and the low frequency selection is ob-
tained by using for each channel a different length L of re-
tarding lines satisfying the relation $\Delta f \, L/c = n = 1,2,3,\ldots$,
already derived in Eq. 40.

The Pulsator multichannel interferometer, described in the following, (c.f. Fig. 2) has 8 vertical probing beams and a horizontal one.

In Fig. 2 a klystron in 3 mm wave range (VARIAN VRB 2111-A, $f_o = 88,5$ Gc/s) or in 2 mm wave (VRT 2122B, $f_o = 150$ Gc/s) feeds 4 channels. The klystron is sawtooth modulated in frequency as stated above. A waveguide is connected to the output of the oscillator; this feeds a "Triple Hybrid Ring" which divides the millimetric wave power into the 4 measuring channels.

Each measuring channel is provided with a retarding line having a path length n times the basic length of the channel 1, where n = 1,2,3 and 4. By using directional couplers part of the incident wave is directed into the reference branch of each channel. Both reference and measuring branches of each interferometer channel are connected to the inputs of a balanced mixer, whose outputs are in turn connected to a differential amplifier, from which the low frequency signals $n \omega_m$ are obtained. Figure 19 shows the modulating sawtooth voltage at a repetition frequency $\omega_m = 100$ kc/s, and the low frequency signals ω_m, $2 \omega_m$, $3 \omega_m$ and $4 \omega_m$ out of the differential amplifiers of the channels 1 to 4.

The low frequency interference signals $n \omega_m$ shown in Fig. 19 a) are displayed through the use of a tuned filter inserted in the differential amplifiers. In Fig. 19 b) the same signals are directly displayed from the various mixers through the use of wide-band differential amplifiers.

By comparison of Fig. 19 a) and b) these low frequency interference signals $n \omega_m$ can be regarded as distortion-free.
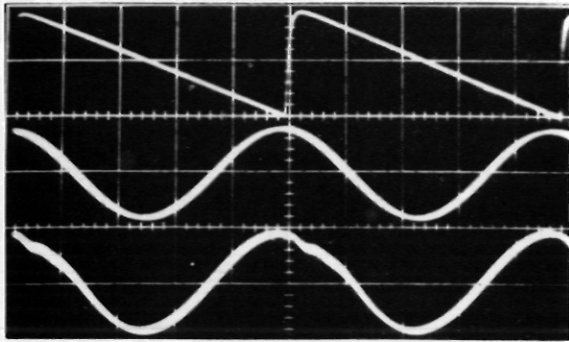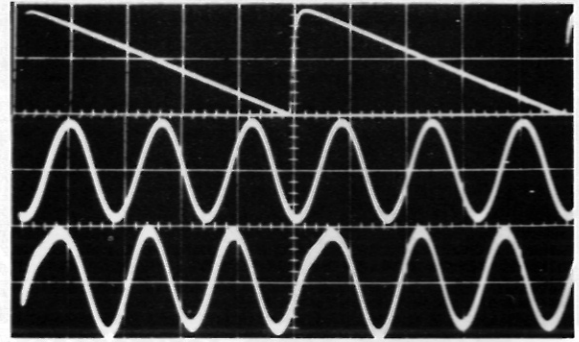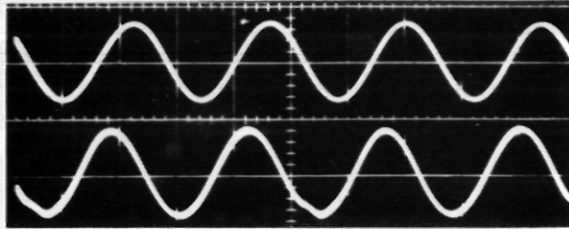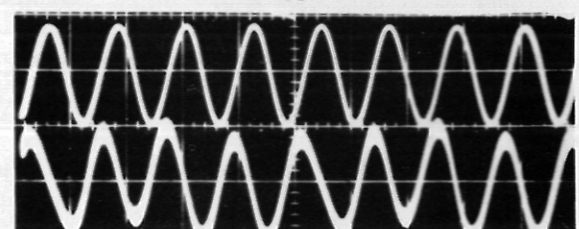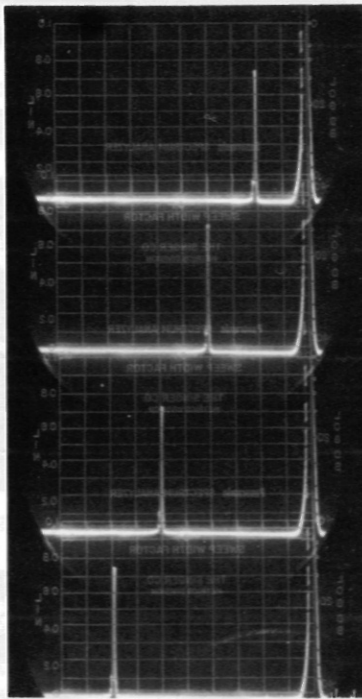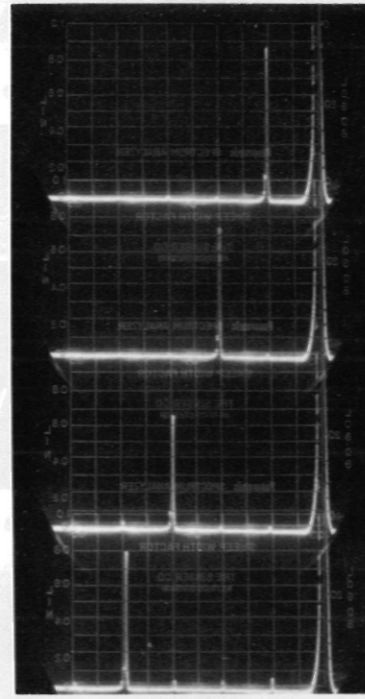
Fig. 19 Sinusoidal interference signals $n\omega_m$

a) Tuned amplifiers

b) Wide-band amplifiers
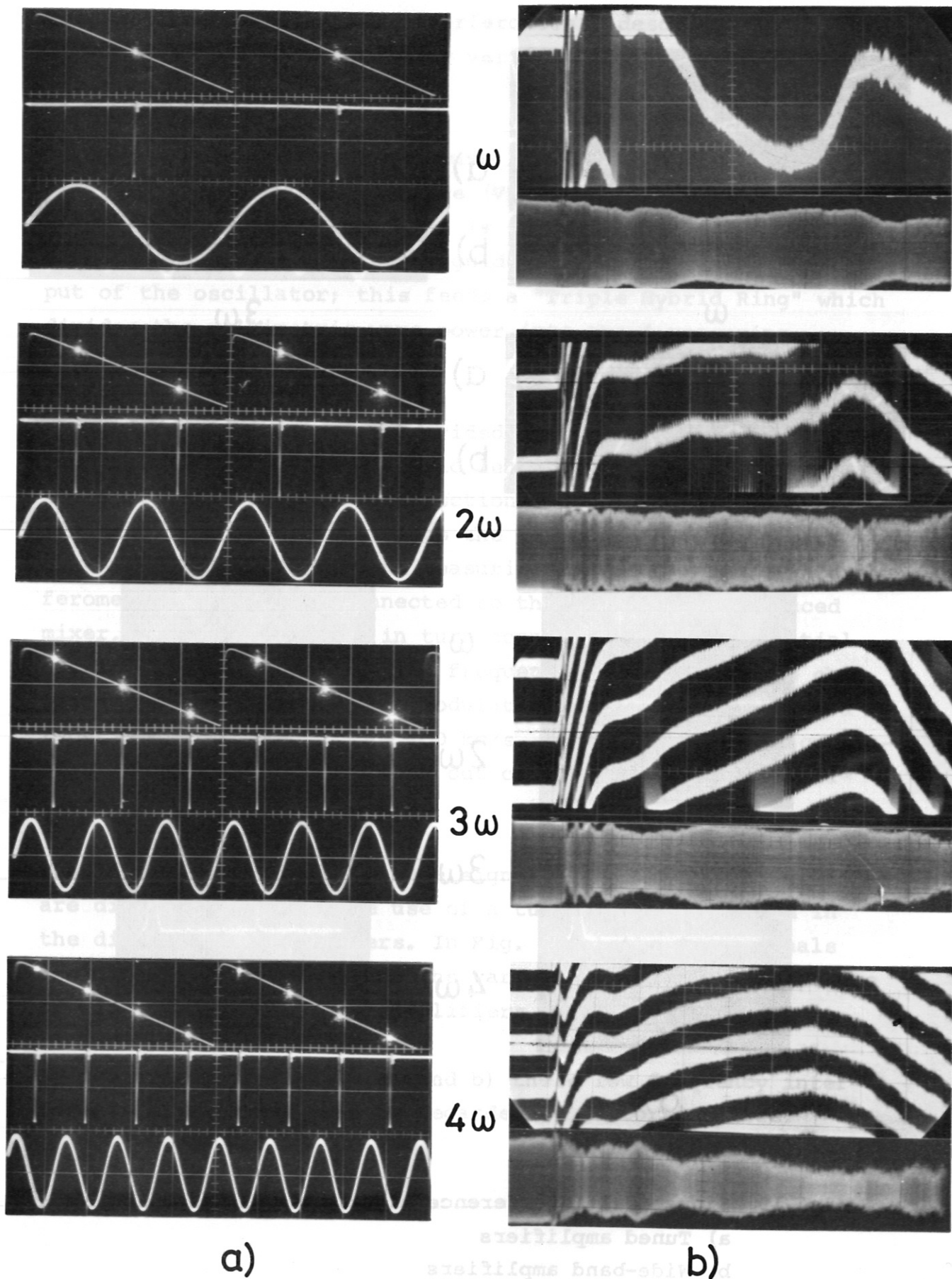
ω

2ω

3ω

4ω

a)

b)

Fig. 20 Fringe shift interference display

As shown in Fig. 20 a), every time the low frequency signals $n \omega_m$ pass through zero, short pulses are initiated. These control the brightness of the cathode ray in the oscilloscope, the y amplifier of which is fed with the sawtooth voltage shown in Fig. 20 a) upper trace.
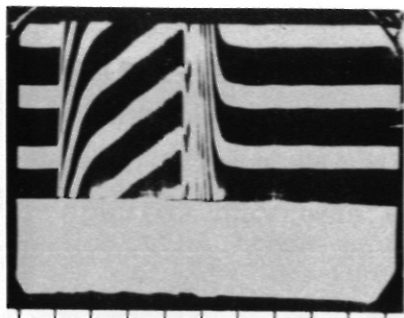
On this sawtooth voltage there then appear n spots corresponding to the low frequency selection $n \omega_m$. If the deflection speed of the oscilloscope is kept sufficiently small compared with the frequency of the modulating signal, the sawtooth periods merge. The n spots then form n lines or fringes, the perpendicular deflection of which (fringe shift) is a measure of the phase shift of the wave, one fringe shift being equal to a phase shift of 2π. The phase display is independent of variations in the amplitude of the wave.

Figures 20 b) upper trace show the fringe shift display of the phase variations of the low frequency interference signals ω, 2ω, 3ω and 4ω for 4 different channels of the interferometer during one discharge shot of the Tokamak Pulsator. In the bottom trace the amplitude variation of these low frequency signals are displayed.

Referring to Fig. 2 a compensating interferometer branch has been inserted in the multichannel interferometer system. This compensating branch is necessary to avoid the random phase shift of the low frequency interference signals due to vibration in the apparatus. In transit time tubes with mechanically tunable resonant circuits, the vibrations cause random variations Δf_o of the carrier wave f_o which in turn produces an unwanted random phase shift $\Delta\varphi$ expressed by:

$$\Delta\varphi = 2\pi \ \Delta f_o / \Delta f$$

where Δf is the sawtooth frequency deviation. In Fig. 2 part
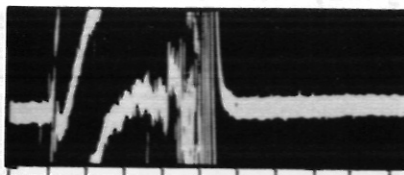
horizontal
channel

phase shift

λ = 2mm

amplitude

t (10 ms/div.) ⟶

Tokamak Pulsator 1

shot nr. 1095

Multichannel Interferometer

vertical channels
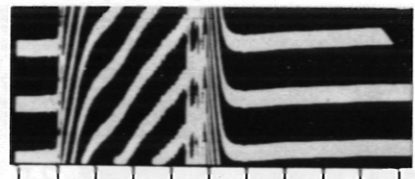
λ = 3.3 mm

t (10 ms/div.) ⟶

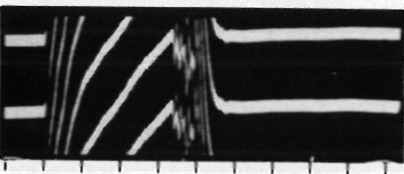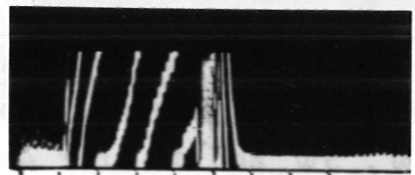t (10 ms/div.) ⟶

limiter inside

ch.1   2   3   4   5   6   7   8

limiter outside
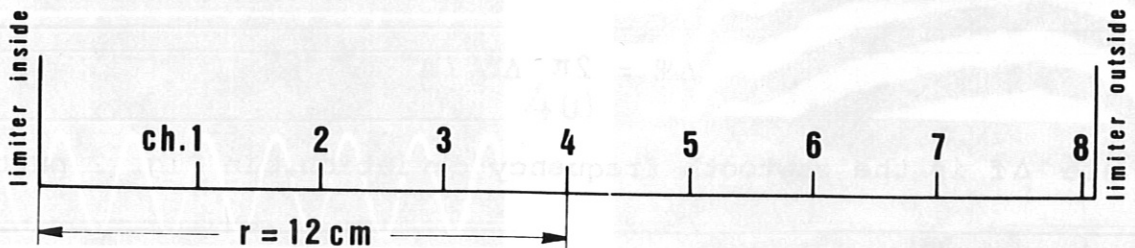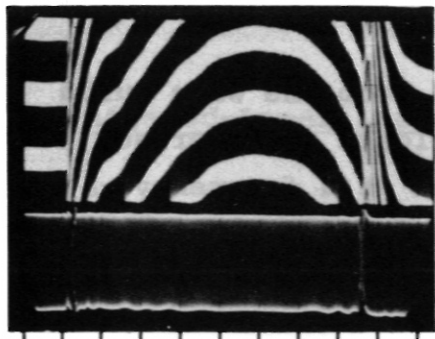
r = 12 cm

Fig. 21 Multichannel Interferograms
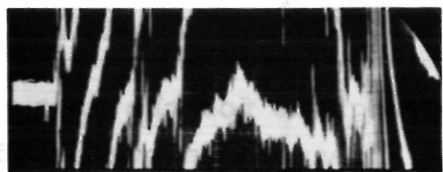
horizontal channel

phase shift

$\lambda = 2\,mm$

amplitude

t (10 ms/div.) ⟶

Tokamak Pulsator 1

shot nr. 1110

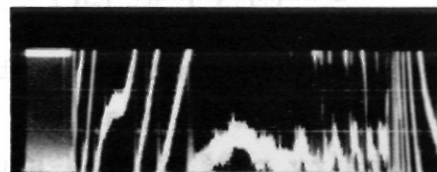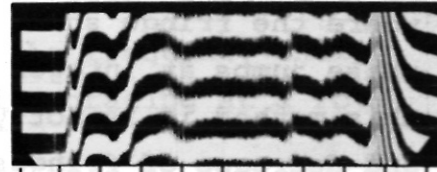**Multichannel Interferometer**

vertical channels

$\lambda = 3.3\,mm$

1

2

3

4

5

6

7

8

t (10 ms/div.) ⟶

t (10 ms/div.) ⟶

limiter inside

limiter outside

ch.1   2   3   4   5   6   7   8

⟵ r = 12 cm ⟶
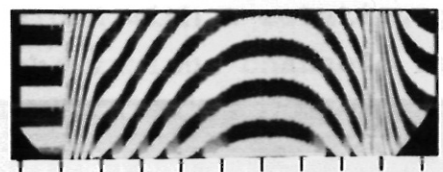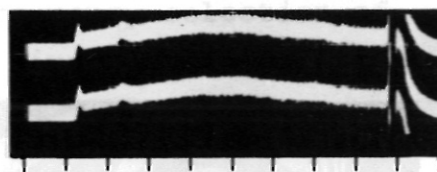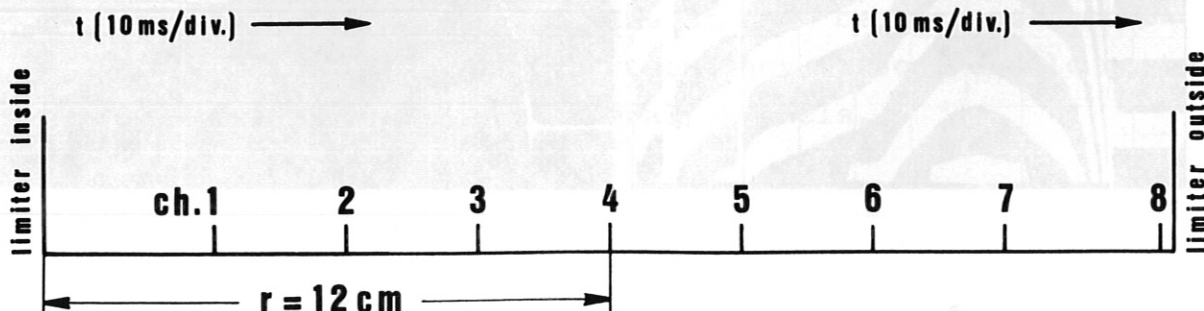
Fig. 22

of the millimetre wave energy is diverted from the wave guide
output of the klystrons and is fed to a closed interference
branch. The sinusoidal interference signal at a frequency ω_m
is fed to the "vector analyser" of Fig. 2, where, synchronised
with ω_m, the sawtooth voltages shown in Fig. 20 a) upper trace
are produced.

These sawtooth voltages are subjected to the same random phase
shift, due to vibrations, as the intensifying impulses of
Fig. 20 a) middle trace, thus cancelling the effect of random
phase shift of the various interferometer channels.

Figures 21 and 22 show two sets of interferograms for the shot
1095 and 1110 respectively. Shot 1095 has already been evaluated
in Fig. 5 a) and b) where the density profiles at the instants of
5,10,20 and 34 ms have been given.

Shot 1110 has been elaborated in Fig. 8 a) and b) where the
new numerical grafical method of Abel's transformation of the
density profiles is shown.

An attempt at automatic fringe counting is shown in Fig. 23 b)
where the fringe shift of Fig. 23 a) is displayed without the
phase jumps at integer of 2π. It should be noted that with
this method it is not yet possible to count the rapid increase
and decrease of fringes number during the disruptive instabili-
ties.
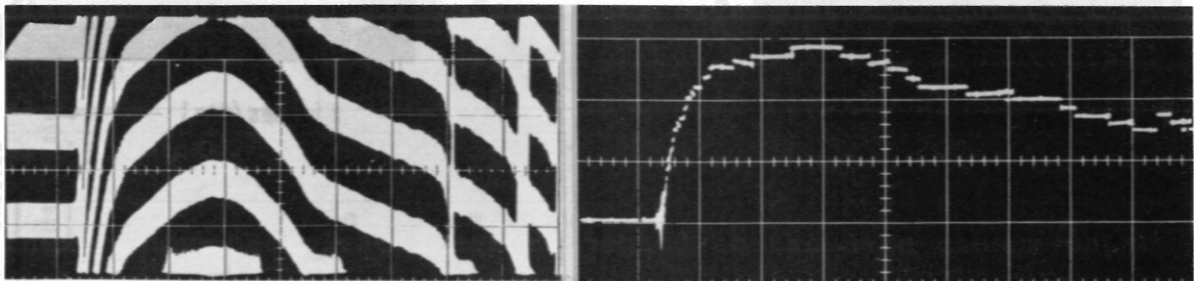
a   b

Fig. 23   Automatic counting of fringes

b) <u>Infrared-Laser interferometer</u>
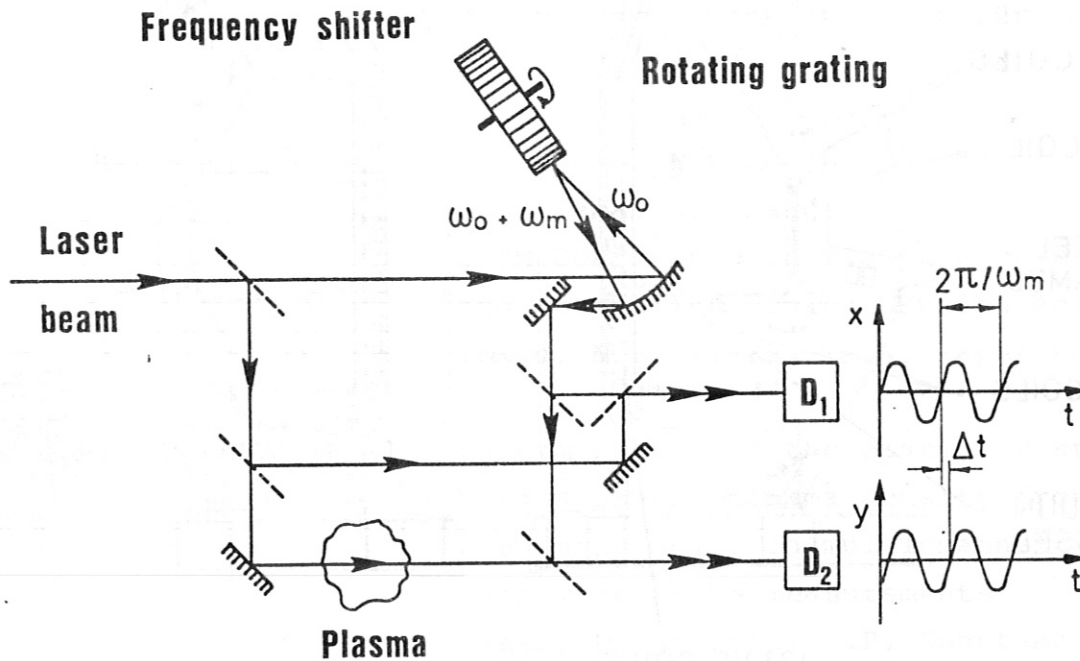
Fig. 24   Schematic of a Laser-infrared interferometer
         (Courtesy of D. VERON)

In Fig. 24 is reported the schematic of a Laser interferometer
given by D. VERON /16/. As noted before the frequency shift
f_m = GN is obtained by means of a rotating grating at a ro-
tational speed N.

For a multichannel interferometer, each channel should be pro-
vided with a rotating grating and the frequency selection of
the various channels can be obtained by simply using different
rotational speeds.

However, because of the large size of both beam cross-section
and rotating grating, it may turn out not to be a simple matter
to extend this circuitry to several channels.
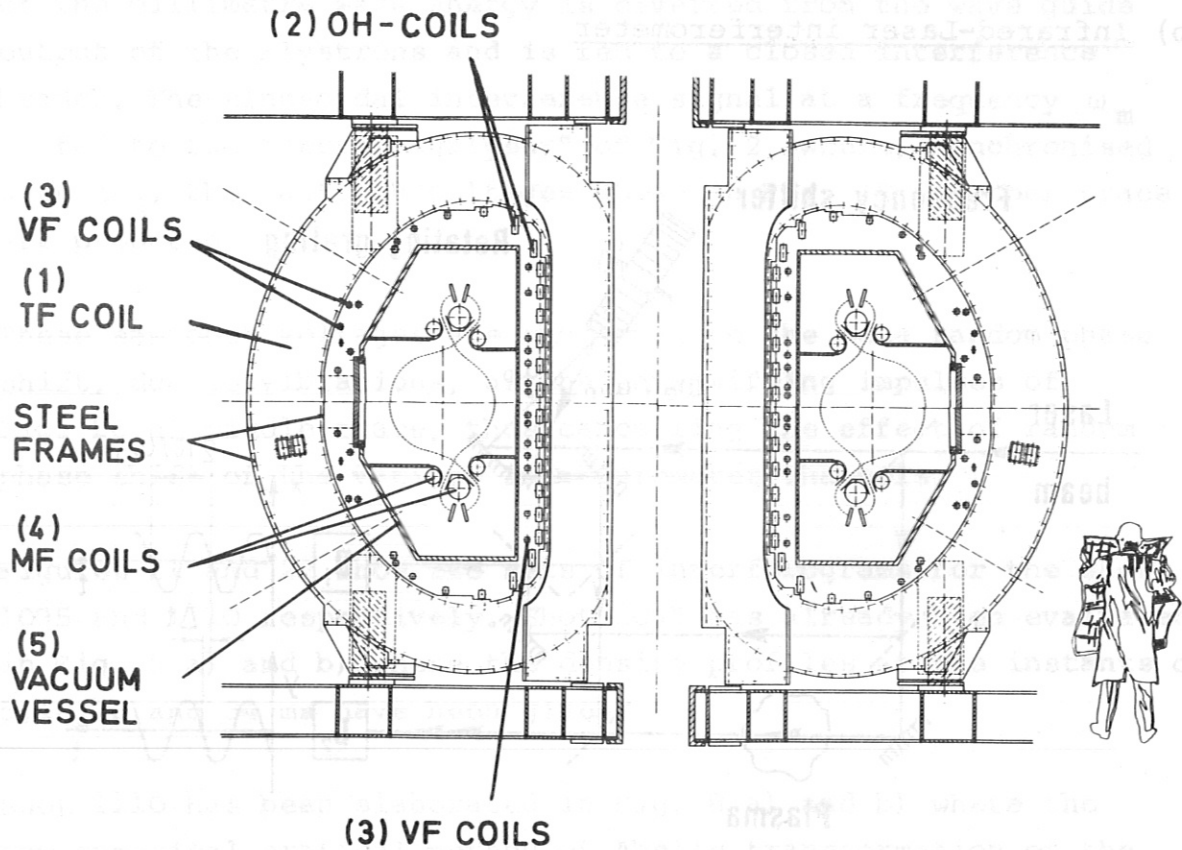
Fig. 25   Cross-section of ASDEX Tokamak

In particular, as seen in Fig. 25 it will not be possible
to use simple-pass (Mach-Zehnder) type interferometer for
the horizontal and for most of the vertical Laser-beams of
the ASDEX Tokamak. By using double-pass (Michelson) inter-
ferometer, on the other hand, one cannot modulate the path
$k_o x(t)$ (c.f. Eq. 41) of the plasma probing beam with the
rotating grating shown in Fig. 24, as has been done in
the interferometer circuitry reported in Ref. /16/. There-
fore, in order to avoid a high level of noise due to plas-
ma scattering and multiple reflection of the Laser-beam,
further development of this interferometer is necessary to
extend it to ASDEX.

Acknowledgement

/1/ O. KLÜBER   Investigation of the equilibrium
and stability behaviour of Tokamak
discharge in Pulsator I
Report Max-Planck-Institut für
Plasmaphysik, IPP III/4 (1974)

/2/ F. KARGER et al   Influence of resonant helical fields
on Tokamak discharges
5-TM Conference on Plasma Physics
and Controlled Nuclear Fusion Research
Tokyo, Nov. 11-15, 1974, Paper PD-2

/3/ E.P. GORBUNOV et al   Determination of the spatial distri-
bution of the plasma density from
the phase shift in multichannel
microwave probe measurements
Plasma Diagnostic, B.P. Konstantinov
Moscow (1963), 68-77

/4/ K. BOCKASTEN   Transformation of radiances into
radial distribution of the emission
of a plasma
Journal of the Optical Society of
America 51, 943 (1961)

/5/ W.L. BARR   Method for computing the radial
distribution of emitters in a cy-
lindrical source
Journal of the Optical Society of
America 52, 885 (1962)

/6/ J.M. MERMET et   Etude de l'inversion d'Abel en vue
    J.P. ROBIN   de la mesure de la répartition de
la température dans un plasma inductif
Rev. int. Htes Temp. e Refract, 10,
(1973)

/ 7/ G. LISITANO,   Determinazione del profilo di den-
     N. GOTTARDI,   sità di un plasma di tipo "Tokamak"
     B. CANNICI et al   mediante interferometria multi-
                        canale ad onde millimetriche
                        "Alta Frequenza" No. 8 Vol. XLIII
                        (1974)

/ 8/ J. SHMOYS   Proposed diagnostic method for cy-
                       lindrical plasmas
                       Journal of Applied Physics - Vol. 32,
                       No. 4, (April 1961)

/ 9/ G.B. WHARTON   Microwave diagnostic for controlled
                       fusion research
                       Report U.C.R.L. - 4836 (1957)

/10/ G. LISITANO   Mikrowellen-Polar-Interferometer für
                       Plasmadichtemessungen
                       Proceedings 5th International Con-
                       ference on Ionisation Phenomena in
                       Gases
                       München, 1, 405-516 (1962)
                       North Holland Publishing Company,
                       Amsterdam

/11/ G. LISITANO   Microwave Dual-Interferometer for
                       Plasma Diagnostic
                       Proceedings 6th International Con-
                       ference on Ionisation Phenomena in
                       Gases
                       Paris, 4, 199-201 (1963)
                       Bureau des Editions Centre d'Etude
                       Nucléaires de Saclay

/12/ G. LISITANO   The application of the sinusoidal
interference method in the design of
a reflectometer and polarimeter in
the range of millimetric waves
Nachrichtentechnische Zeitschrift,
Communication Journal 14, 103-107
(1963)

/13/ G. LISITANO   Verfahren und Einrichtung zur fort-
laufenden Messung der Änderung eines
komplexen Übertragungsmaßes oder Re-
flexionsfaktors
Deutsches Patent Nr. 1 139 204 (1960)

/14/ G. LISITANO   Automatic phase-measuring system for
a 8 mm carrier wave and its 4 mm-
harmonic
Review of Scientific Instruments 36,
364-367 (1965)

/15/ P. BELLAND and   A compact CW HCN Laser with high
     D. VERON   stability and power output
Optics Communication 9, 146 (1973)

/16/ D. VERON   High sensitivity HCN Laser interfero-
meter for plasma electron density
measurements
Optics Communications 10, 95 (1974)